

STATE RESEARCH CENTER OF RUSSIA
INSTITUTE FOR HIGH ENERGY PHYSICS

**Advanced Conceptual Design of the Full Scale Fin Target
and Engineering Design of the Target Prototypes
for the NuMI Project**

(Task C Report of the Accord between FNAL and IHEP)

A.Abramov, I.Azhgirey, P.Galkin, N.Galyaev, V.Garkusha,
V.Gres, V.Ferapontov, I.Kurochkin, F.Novoskoltsev,
A.Ryabov, V.Zapolsky, V.Zarucheisky

Protvino 1998

Contents

1	Full Scale Target	3
1.1	Properties of Target Materials	3
1.1.1	Graphite	3
1.1.2	Beryllium	5
1.2	Proton Beam Distribution	7
1.3	Calculations of the Energy Deposition in the Target	8
1.4	Temperature and Stress Calculations	9
1.4.1	Temperature Calculations	9
1.4.2	Thermal Stresses in the Target. Choice of a Tooth Length	10
1.5	Longitudinal Structure of the Target	11
1.6	Transverse Beam Scan Across the Target	11
1.7	Full Scale Target Design	12
1.7.1	General Description of the Target Design	12
1.7.2	Energy Deposition in Different Parts of the Target	13
1.7.3	Cooling System of the Target	13
1.8	Comparison of Various Target Designs	14
1.9	Conclusions	15
2	Target prototypes	34
2.1	General Description of the Target Prototype Design	34
2.2	Operation Conditions of the Prototype Testing. Thickness of the Target Piece	35
2.3	Beam Spot Sizes for Prototypes Testing	36
2.4	Temperature and Quasistatic Thermal Stress Considerations	37
2.5	Summary	40
3	Neutrino Beam Optics	55
3.1	Low Energy Wide Band Beam	55
3.2	Narrow Band Beam	57

1 Full Scale Target

In this Section the conception of water cooled graphite and beryllium targets for the NuMI is represented taking into account "real" distribution of the proton beam in transverse direction. The choice of a target material is discussed as well as energy deposition; temperature and stress distributions in graphite and beryllium targets are represented. The geometry of the target segment was chosen from the analysis of stresses caused by irradiation of the target by the proton beam. Calculations of stresses as functions of the transverse beam location on the target show that their values are substantially lower than ultimate strength characteristics of the target material. The longitudinal structure of the full scale target was obtained from the calculations of a total neutrino event rate at the MINOS far detector for the wide band neutrino beam. The design of the full scale target is given. The cooling system was determined from calculations of the energy deposition in different units of a target design. The comparison of production efficiencies for various types of targets is done.

1.1 Properties of Target Materials

As possible materials for targets we consider graphite and beryllium. The properties of these materials vary with the temperature, and so it should be taking into account under the temperature and stress calculations.

1.1.1 Graphite

The number of graphite materials is very wide. Among the suppliers of uniform graphite materials Poco Graphite, Inc. is the most well known all over the world. From a variety of Poco Graphite grades ZXF-5Q grade is the most suitable for the target production because it has highest mechanical strength, lowest particle and pore sizes [1]. The typical properties of ZXF-5Q grade are listed in Table 1.1.

The strength characteristics of ZXF-5Q increase with a temperature rise contrary to usual metals. This increasing is essential when the operating temperature is more than 1000°C but under the temperature below 600–700°C it may be neglected [2]. The product of a thermal expansion coefficient and modulus of an elasticity linearly increases by 1.6 times from a room temperature to 1000 °C whereas specific heat C_p of ZXF-5Q graphite

increases by factor two in this temperature range and may be described by the formula $C_p \simeq -3462 + 741 \cdot \ln T$, J/kg/K. No data on fatigue stress limit of ZXF-5Q grade are available.

Melting Point	3600 °C
Sublimation Point	3320 °C
Particle Size	1 μm
Total Porosity	20%
Pore Size	0.3 μm
Density	1.81 g/cm ³
Compressive Strength	195.0 MPa
Flexural Strength	115.0 MPa
Tensile Strength	90.0 MPa
Modulus of Elasticity	14.5·10 ³ MPa
Tensile Strain to Failure	0.78%
Poisson Ratio	0.2@1000°C
Hardness SSH	86
Thermal Conductivity	70 W/m/K
Coefficient of Thermal Expansion	7.7·10 ⁻⁶ 1/K
Specific Heat	714 J/kg/K

Table 1.1: Room temperature properties of ZXF-5Q Grade.

As it was shown in our previous report [3], the efficiency of the fin target increases if its thickness is lower than diameter of the cylindrical target and the beam spot has an elliptical shape ($\sigma_y \simeq 2\sigma_x$). It means that the thickness of the graphite target should be less than 4 mm (diameter of the graphite target with helium cooling). It is convenient to take $d = 3.2$ mm, where d is the thickness of the target fin, because Poco supplies precision ground plates with such thickness. Preliminary design of the full scale target with cooling of the target fin on the lateral surfaces shows that the height of the target segment should be at least 120 mm. Poco supplies precision ground plates 100×150 mm². So the length of the target piece along the beam equal to 100 mm is quite reasonable in view of minimal machining of the graphite plate.

As it will be shown below the luminosity of the target with such thickness and target segment length is comparable with the cylindrical one.

1.1.2 Beryllium

The variety of beryllium materials is also very wide. One of the best suppliers of high quality beryllium grades is Brush Wellman, Inc.. The study of published data of Brush Wellman materials [4, 5] shows, that VHP (Vacuum Hot Pressing) grades S-200F and S-65C may be used as possible grades for the beryllium target. Both grades have the same typical room temperature properties listed at Table 1.2. For these grades there are the most full data of their properties including fatigue stress testing.

Melting Point	1284°C
Grain Size	$\leq 20 \mu\text{m}$
Density	1.82 g/cm ³
Ultimate Tensile Strength	372 MPa
Yield Strength	261 MPa
Modulus of Elasticity	312·10 ³ MPa
Poisson Ratio	(0.06–0.10)@20°C
Thermal Conductivity	199 W/m/K
Coefficient of Thermal Expansion	10.7·10 ⁻⁶ 1/K
Specific Heat	1770 J/kg/K

Table 1.2: Room temperature properties of S-65C Grade.

The characteristics of beryllium vary with temperature too, as it is shown in Figure 1.1a. But if the strength of a graphite may increase with temperature, the ultimate tensile strength, as well as the yield strength of beryllium, drops with temperature as it is shown in Figure 1.1b. The variation of material properties should be taken into account at the temperature and stress computations.

Fatigue data on S-200F are the most complete available for structural beryllium grade. In Krause rotating beam fatigue tests, S-200F shows that there are no difference in the 10⁷ cycle endurance limit in the longitudinal and transverse directions. That means components can be expected to undergo 10⁷ cycles from -261 to +261 MPa without failure, that is remarkable in view of a specification yield stress equal to 261 MPa. This means one can use yield stress as a primary design criterion for fatigue considerations [4]. Fitting of data [5] on fatigue tests at room temperature of S-200F (1.06%

of BeO content) shows, that the fatigue endurance limit σ_{-1} as function of number of cycles N may be described as $\sigma_{-1}(N) = S_{\infty} + S_1 / (\log N)^m$, where $m = 13-14$, $S_{\infty} \simeq 262.3$ MPa for longitudinal and $m = 8-9$, $S_{\infty} \simeq 260.3$ MPa for transverse directions respectively. Calculations on this formula for the life time $5 \cdot 10^7$ cycles give the minimal endurance limit in the transverse direction $\sigma_{-1} = 261.6$ MPa. If the σ_{-1} varies with temperature similar to ultimate tensile and yield stresses (see Figure 1.1b), than for the operating temperature 220°C and the life time $5 \cdot 10^7$ cycles σ_{-1} should have the value of $\sigma_{-1}(220^{\circ}\text{C}) = \sigma_{-1}(20^{\circ}\text{C}) \cdot 0.83 = 217.1$ MPa. Taking into account the value of the fatigue ratio of S-200F (ultimate tensile strength – to fatigue endurance limit), which is equal to 0.7 [4], the ultimate tensile strength for the beryllium target should not exceed 152 MPa.

As it was mentioned above the both grades (S-200F and S-65C) are VHP grades. S-65C is practically similar to S-200F, but is more pure grade (see Table 1.3 of [4]).

Grades	S-200F	S-65C
Beryllium Assay, %, min.	98.5	99.0
Beryllium Oxide, %, max.	1.5	1.0
Aluminum, %, max.	0.1	0.06
Carbon, %, max.	0.15	0.1
Iron, %, max.	0.13	0.08
Magnesium, %, max.	0.08	0.06
Silicon, %, max.	0.06	0.06
Other metallic impurities, %, max.	0.04	0.04

Table 1.3: Chemical composition of S-200F and S-65C Grades.

It may be expected that fatigue limit of S-65C for typical values of the strength characteristics is similar to S-200F. On the other hand, S-65C has the best resistance to crack initiation and crack propagation depth in comparison with S-200F (see Table 1.4 of [6]).

The initiation of cracks as well as its propagation are strongly depend on the surface quality of a target piece. Machined surfaces are usually damaged by the formation of twins and/or microcracks. The depth of the damage depends on the machining process, the sharpness of the tool, the rigidity of the setup and the grain size of the beryllium. To minimize the depth

of machining damage there is the standard practice of chemical etching of 2÷4 mils from all machined surfaces [7]. After chemical etching the target piece should be degreased by means of an industrial grade, water based degreaser, then rinsed with acetone and methanol.

Beryllium grade	S-200F	S-65C
Number of cycles to crack initiation	1300	2400
Crack propagation depth, mm	1.2	0.3

Table 1.4: Crack initiation and its propagation depth of S-200F and S-65C Grades.

S-65C grade has the greatest value of elongation (3%) at room temperature among all known beryllium grades; it is very important to the passage of a target from the room to the steady state temperature. So, taking into account typical values of strength characteristics, the results of the crack initiation test and the crack propagation depth, S-65C is more preferable than S-200F grade.

It should be noted that a beryllium has a very high modulus of an elasticity, which is 20 times higher than that for graphite. This is the main reason why the beryllium target should operate at the temperature which is significantly lower than graphite one i.e. the thickness of the beryllium target and consequently the beam spot sizes should be larger than that for graphite target. As it was shown in [3] the thickness 4.1 mm of the beryllium fin target is closed to optimal. In order to have the target design compatible for both types of the target material it is convenient to take the length of the target segment along the beam equal to 100 mm. So, the 4.1 mm thick and 100 mm length piece of the beryllium segment is taken for further computations of energy depositions and consequently of thermal stresses.

1.2 Proton Beam Distribution

Distributions of the energy deposition in a cross section of the target as well as that of stresses in a target segments strongly depend on the transverse proton beam distribution on the target. The analysis of data received by a Monte Carlo simulation of a proton beam transport to the NuMI target given by the FNAL [8] shows that at present statistics:

- the proton beam is essentially non-symmetrical in a horizontal plane (X-direction) and may be described well by the 4-th order polynomial $N(x) = \sum_{k=0}^4 \alpha_k \cdot x^k$ (Figure 1.2a). Coefficients α_k are computed with help of linear fitting of data. If the first momentum of this distribution is equal to zero (i.e. the beam is centered with respect to the target), then the left and right roots of polynomial, defining the beam width, are different by the absolute values. Scaling from the given beam width to the new one may be made using the standard deviation of both distributions.
- the beam distribution in a vertical plane (Y-direction) is very similar to the Gaussian (Figure 1.2b). The Gaussian parameters of distribution shown in Figure 1.2b were computed directly from the Monte Carlo simulation data.

Such distributions in horizontal and vertical planes were used for calculations of energy deposition densities and consequently of stresses in a target. The parameters of a primary proton beam on the target, used for further consideration are given in Table 1.5.

Beam energy	120 GeV
Pulse duration	1.0 ms
Repetition period	1.9 s
Number of protons per spill	$4 \cdot 10^{13}$
Beam distribution in X-direction	non-Gaussian
Beam distribution in Y-direction	\sim Gaussian

Table 1.5: Parameters of the primary proton beam.

1.3 Calculations of the Energy Deposition in the Target

The energy deposition in a target was computed by MARS [9] using "real" proton beam distributions described in a previous subsection. The proton beam is centered in X-direction with respect to the plane of the target symmetry in such a way, that the first momentum of a distribution is equal to zero. The gap between left edges of a beam and a target piece is chosen to 0.15 mm. The transverse distribution of the energy deposition density was averaged along the target piece. Parameters of targets and the proton beam considered for energy deposition calculations are given in Table 1.6.

Target material	Graphite	Beryllium
Length of the target piece, mm	100	100
Thickness, mm	3.2	4.1
σ_y of Gaussian beam, mm	1.28	2.0
Location of a beam center from the upper end of the target, mm	2.808	4.1
Equivalent σ_x in X-direction, mm	0.673	0.879
Beam width in X-direction, mm	2.76	3.614
Gap between left edges of the beam and the target piece, mm	0.15	0.15

Table 1.6: Geometrical parameters of the proton beam and the target.

Transversal distributions of densities of the energy deposition are shown in Figures 1.3a (graphite target) and 1.3b (beryllium target). The origin of coordinate system ($x = y = 0$) corresponds to the proton beam center. The maximum energy deposition density is equal to $0.109 \text{ GeV/cm}^3/\text{p}$ for the graphite target and $0.0563 \text{ GeV/cm}^3/\text{p}$ for the beryllium one. The analysis of a distribution of the energy deposition in X-direction shows, that its first momentum (at $y = 0$) is equal to $\sim 0.1 \text{ mm}$ due to the non-symmetry of the distribution of the primary proton beam.

1.4 Temperature and Stress Calculations

The temperature distributions and thermal stresses in a fin target were computed by the finite element program HAST [10]. The model of the target piece (tooth) with length L_t used for temperature and stress calculations by HAST is shown schematically in Figure 1.4.

1.4.1 Temperature Calculations

The temperature calculations were made under the following boundary conditions:

- heat transfer coefficient to water is equal to $10 \text{ kW/m}^2/\text{K}$;
- thermoresistance between the target piece and aluminum base and pressing plates is equal to zero;

- ambient temperature is equal to 20°C;
- radiation is taking into account for coefficient of blackness equal to one;
- heat transfer coefficient to ambient He atmosphere (α_a) is equal to 50 W/m²/K. Calculations show that such value of α_a decreases the target piece temperature in $\sim 10^\circ\text{C}$ with respect to $\alpha_a = 0$ (vacuum).

The temperature distributions in the target along the vertical axis y ($x = 0$) just before and after the beam spill at a steady state are shown in Figure 1.5a and 1.5b for graphite and beryllium targets respectively. The steady state is reached in 30–50 proton spills. The maximum temperature T_{\max} and adiabatic temperature jump ΔT for targets are listed in Table 1.7.

Target material	Graphite	Beryllium
Maximum temperature, T_{\max}	508°C	219°C
Temperature jump, ΔT	279°C	82°C

Table 1.7: Operational temperatures of targets.

1.4.2 Thermal Stresses in the Target. Choice of a Tooth Length

Each segment of the target is cut several times in the vertical direction into subsegments (teeth) in order to minimize the quasi-static thermal stresses in a target. Equivalent stresses in different critical points of a target tooth (see Figure 1.4): 1 – (0;0;0), 2 – (+d/2;0;0) and 3 – (0;0; $\pm L_t/2$) as functions of the tooth length are represented in Figures 1.6a (graphite) and 1.6b (beryllium). As follows from these plots, the most critical point, where the equivalent stress has its maximum value, is the point (+d/2;0;0). In this point:

- the equivalent stress in the graphite target increases with the length of the target tooth. The length of the tooth may be defined in view of machining of the target segment reserving the acceptable level of the equivalent stress. If we'll take the length of tooth equal to 18.4 mm, then we'll have 5 teeth with 2 mm gaps between them and the value of the equivalent stress is equal to 24.8 MPa.

- the equivalent stress in the beryllium target has minimum value at the length of the tooth equal to 10 mm. Taking into account a low growth of the equivalent stress with increasing of the tooth length, at the length of the tooth equal to 12.57 mm we'll have 7 teeth with the 2 mm gap between them and the equivalent stress equal to 152 MPa.

1.5 Longitudinal Structure of the Target

The longitudinal structure of the full scale target (the number of target segments and the distance between them) was chosen from the neutrino event rate calculations at the far detector for the H6.6 wide band beam [11]. The results of these calculations are given in Figure 1.7. One can see that the target with ten ($n = 10$) segments has the efficiency 2% larger than for $n = 9$. On the other hand the passage from $n = 10$ to $n = 11$ gives only 1% growth of a target efficiency. It is quite reasonable to take number of segments equal to ten ($n = 10$) and the distance between segments equal to 75 mm.

1.6 Transverse Beam Scan Across the Target

Using the longitudinal structure of the target, calculations of the energy deposition in the target teeth have been made in order to define the tooth which has the maximum value of a temperature. For this tooth (the last tooth of the first segment in the graphite target and the first tooth of the third segment for beryllium one) the transverse beam scan in the X-direction was made to investigate stresses arose in a target when the beam is not centered with respect to the target. The calculations were carried out for a steady state (the most difficult situation).

Two-dimensional distributions of stresses in these teeth for the case when the beam is centered well in the target, i.e. the beam center-weight coincides with the center of the target are shown in Figure 1.8 (for the graphite target) and in Figure 1.9 (for the beryllium target). Distributions of an equivalent stress in YZ-plane for $x = d/2$ are shown in Figure 1.10a for the graphite target and in 1.10b for the beryllium one. As it follows from Figure 1.10 there is the stress concentration at the corner ($x = \pm d/2$, $z = \pm L_t/2$). In order to avoid the stress concentration, this corner should be rounded.

Stresses in most crucial points ($\pm d/2; 0; 0$) as functions of a beam location are shown in Figures 1.11 for the graphite target and in Figures 1.12 for the beryllium one. As it follows from these plots, values of stresses are higher than that when the beam is centered well, but they are much more lower than ultimate tensile and yield strength of target materials. Taking into account that the beam is deflected from the center of the target only during very short period of a time, the target will withstand such value of stresses without breaking.

1.7 Full Scale Target Design

1.7.1 General Description of the Target Design

The design of the full scale target is shown in Figures 1.13–1.15 (two first segments and the last segment) and in the drawing BLT.dwg enclosed to this Report. Beryllium (or graphite) segment is pressed between the aluminum base and pressing plates (Figure 1.13). A necessary force is provided by two springs for one target segment. The fin is fixed in a vertical position by two small ceramic cylindrical pins. The base plate is clamped to the mounting plate (Al alloy similar to 6061–T6) with four screws.

Cooling water passes through holes in base and pressing plates with inside diameter equal to 8 mm. Base plates of segments are connected by means of aluminum pipes with inside diameter equal to 8 mm welded to the base plates. This system of an assembly can not be used for pressing plates because it can not provide a good thermal contact between the target piece and the pressing plate due to rigidity of the assembly.

The flexible bellows are used in order to decrease the rigidity of the pressing plates assembly. Using of stainless steel bellows demands a special transition from an aluminum to a stainless steel. Such transition may be made by the technology used in the similar transition for hot zones of nuclear reactors [12].

Aluminum details (base, pressing and mounting plates) are anodized with alumina ($40 \mu\text{m}$ thick) in order to provide the insulation of the target fin for the "Budal" monitor.

The mounting plate with all details assembled on it is inserted into stainless steel tube and clamped to two plates, welded to the internal surface of the stainless steel tube. Special screw placed at the center of the target is

used for compensation of the mounting plate sagitta. Two flanges with two beryllium windows separate the internal volume from the surrounding environment. The diameter of upstream beryllium window is equal to 35 mm, whereas the diameter of downstream window is defined by the angle of secondaries and is equal to 170 mm. A perspective view of the full scale target design is shown in Figure 1.16. The cooling water passes initially through the base (or pressing) plates and returns through the holes in a mounting plate.

1.7.2 Energy Deposition in Different Parts of the Target

Calculations of the energy deposition in different units of the target design were made by program MARS'96 [13]. Similar calculations carried out earlier for the eight segment targets show, that total energy depositions in different units practically do not depend on the target material. Therefore calculations were made for the graphite target. The results of calculations for the graphite target in terms of longitudinal distributions of the average power are represented in Figure 1.17 for target segments, base, pressing and mounting plates, as well as for stainless steel external tube. For the external tube the angular distribution of the energy deposition was computed too (see Figure 1.18) in order to make in future the full analysis of its deformation. The total average deposited power in different units of the target design are given in Table 1.8. As it follows from this Table the total power deposited in the mounting plate of the target design is equal to 1.23 kW and it should be water cooled too.

Target segments	1.54 kW
Pressing and base plates	0.874 kW
Mounting plate	1.23 kW
External stainless steel tube	1.62 kW

Table 1.8: The average deposited power in different units of the target.

1.7.3 Cooling System of the Target

Water cooling system should provide the heat transfer coefficient to water equal to 10 kW/m²/K. The heat transfer coefficient α_w can be computed by the following expression

$$\alpha_w = Nu \cdot \lambda/d,$$

where Nu is the Nusselt number, d is the diameter of the water channel, λ is the water thermal conductivity. The Nusselt number is defined from Reynolds (Re) and Prandtl (Pr) numbers by semi-empirical formula [14]

$$Nu = 0.018 \cdot Pr^{0.43} \cdot Re^{0.8},$$

which is true for $10^4 \leq Re \leq 10^6$. Calculations show that for 8 mm diameter of the cooling channel under velocity of the water equal to 3 m/s ($Re = 2.2 \cdot 10^4$) the heat transfer coefficient $\alpha_w = 10 \text{ kW/m}^2/\text{K}$. The total water flow rate is equal to 18 l/min under pressure drop equal to 1.6 atm. The total average power transferred to water is equal to 3.65 kW and the ΔT of the water is approximately 3°C.

1.8 Comparison of Various Target Designs

Production efficiencies of graphite and beryllium fin targets described in this Section with respect to the production efficiency of the 8 segments graphite rod target [15], are shown in Table 1.9. The total neutrino event rates at the MINOS far detector given in this Table have been calculated for the H6.6 three horns focusing system using the Fermilab GNUMI beam simulation software.

Proton beam spot shape	Target design		
	C-rod, 8 segms	C-fin, 10 segms	Be-fin, 10 segms
An axial symmetric and inside the target	3753	3668	3549
The resonant extrac- tion spot shape	3469	3571	3493

Table 1.9: The total neutrino event rates for different target designs.

In a case of an axial symmetric profile of the proton beam located entirely inside the target (perfect focusing of the proton beam), graphite and beryllium fin targets give the total neutrino event rate 0.98 and 0.95 with respect to the "reference" graphite rod target. Because of the resonant extraction scheme, the proton beam spot shape is Gaussian in the vertical direction while its non-symmetric horizontal profile has no tails (see Figure 1.2). For these more realistic proton beam distributions the rod

target loses some part of the proton beam which is expected to be in the Gaussian vertical tails. Otherwise, the vertically oriented fin targets intercept (97–98)% of protons and, as a result, their production efficiency is somewhat higher than that for the graphite rod target.

1.9 Conclusions

The advanced conceptual design of the full scale target described in this Section corresponds to the NuMI beam intensity of $4 \cdot 10^{13}$ protons per spill. It is evidently that for intensity of $6 \cdot 10^{13}$ protons per spill the targets with the thicknesses 3.2 mm (graphite) and 4.1 mm (beryllium) can not be used due to noticeable (by factor of 1.5) increase of stresses. For such intensity an additional optimization of the target piece thickness should be done taking into account the total neutrino event rate at the far detector.

In order to verify the general conception described above, the full analysis of deformations of the target design will be made in July–September.

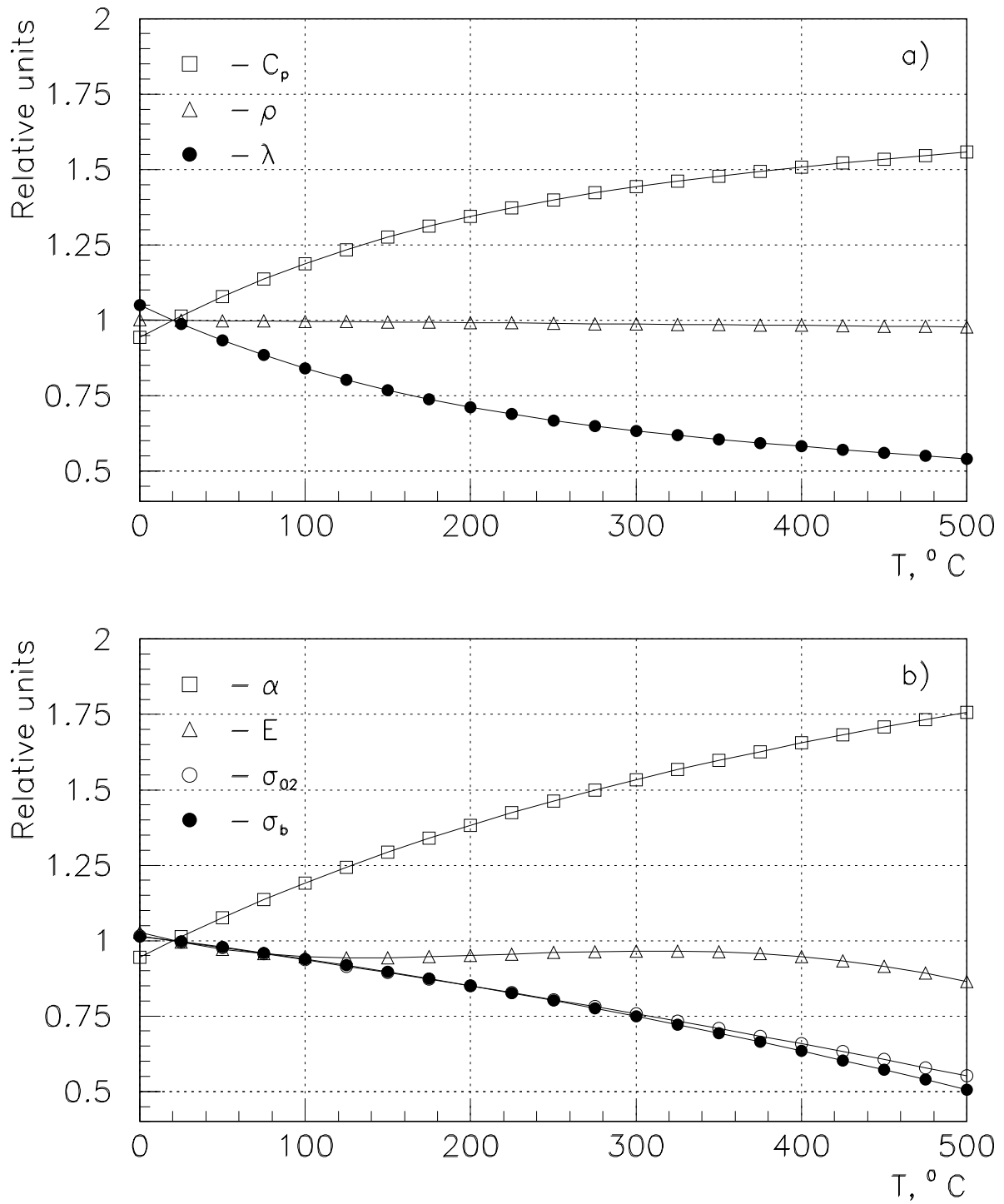


Figure 1.1: S-65C properties as functions of temperature, normalized to ones at 20°C: a) C_p – specific heat, ρ – density, λ – thermal conductivity; b) α – coefficient of thermal expansion, E – modulus of elasticity, σ_{02} – yield strength, σ_b – ultimate tensile strength.

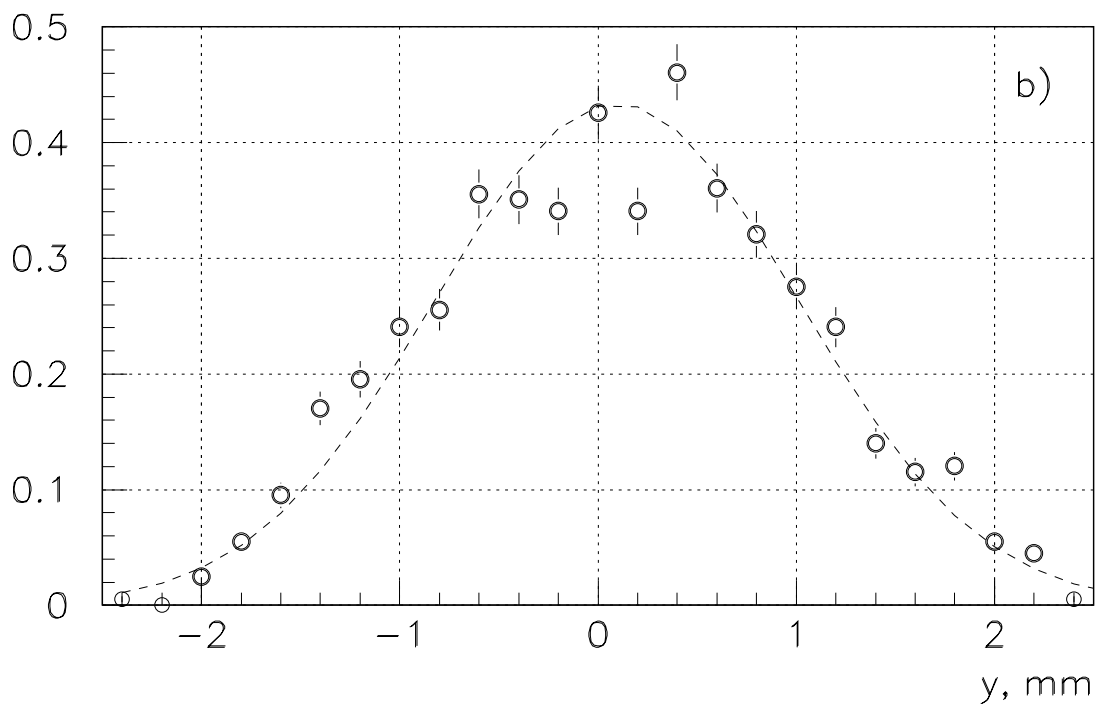
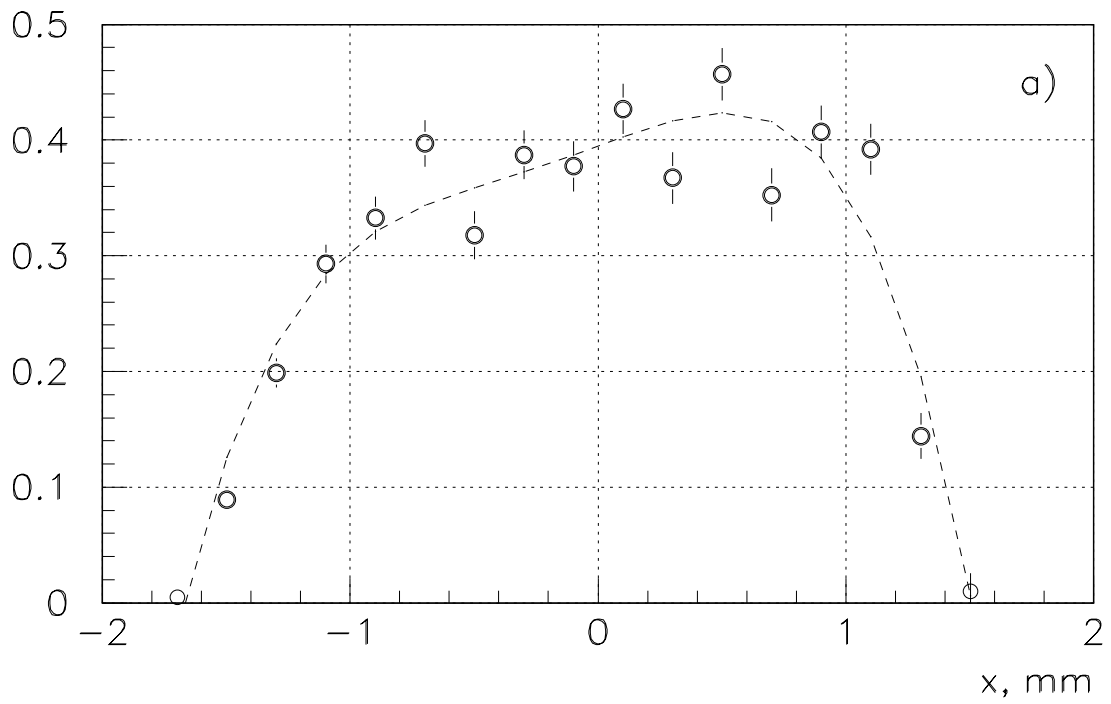
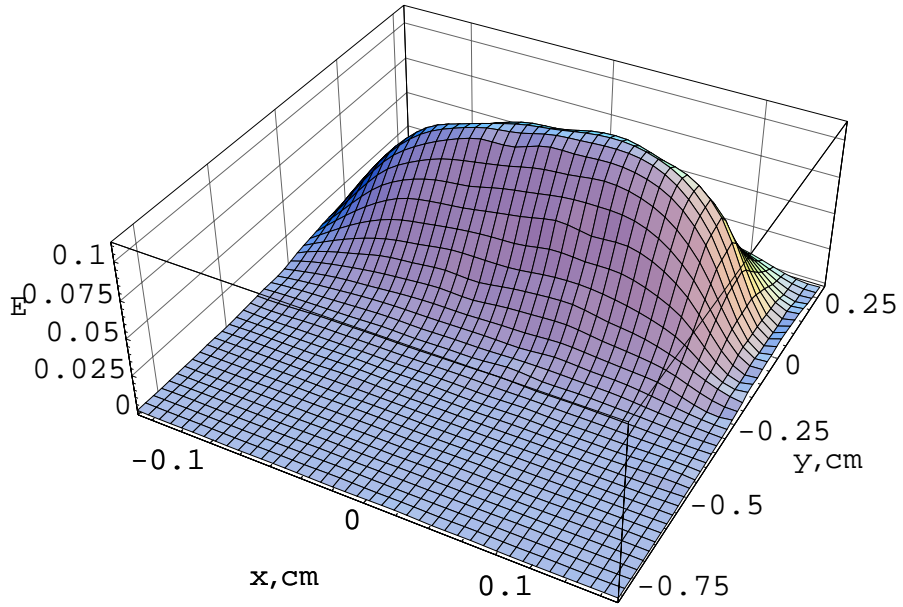
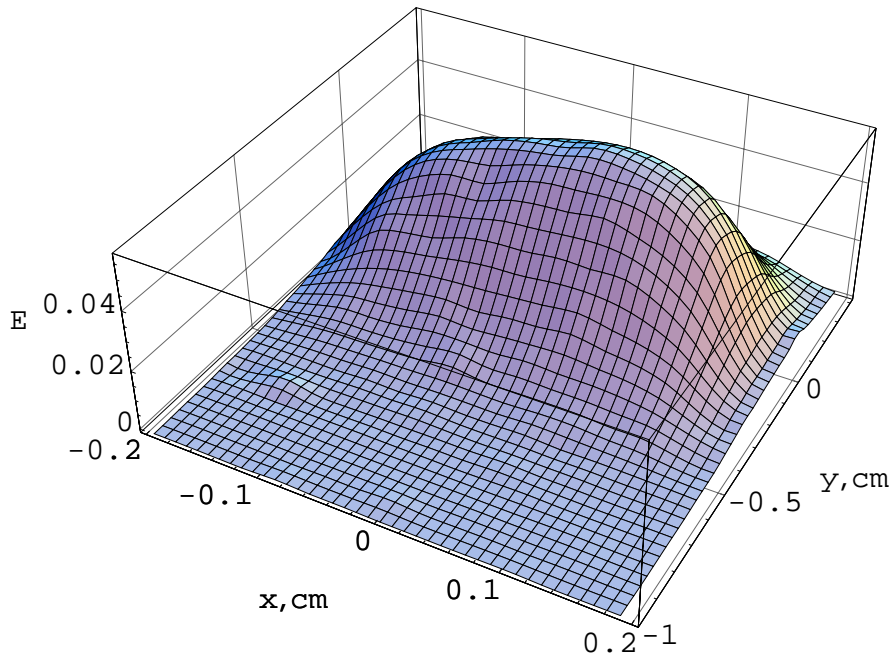


Figure 1.2: Normalized transverse beam distributions:
a) X-direction; b) Y-direction.



a)



b)

Figure 1.3: Transversal distributions of the energy deposition density: a) graphite target; b) beryllium target. E is given in $\text{GeV}/\text{cm}^3/\text{p}$.

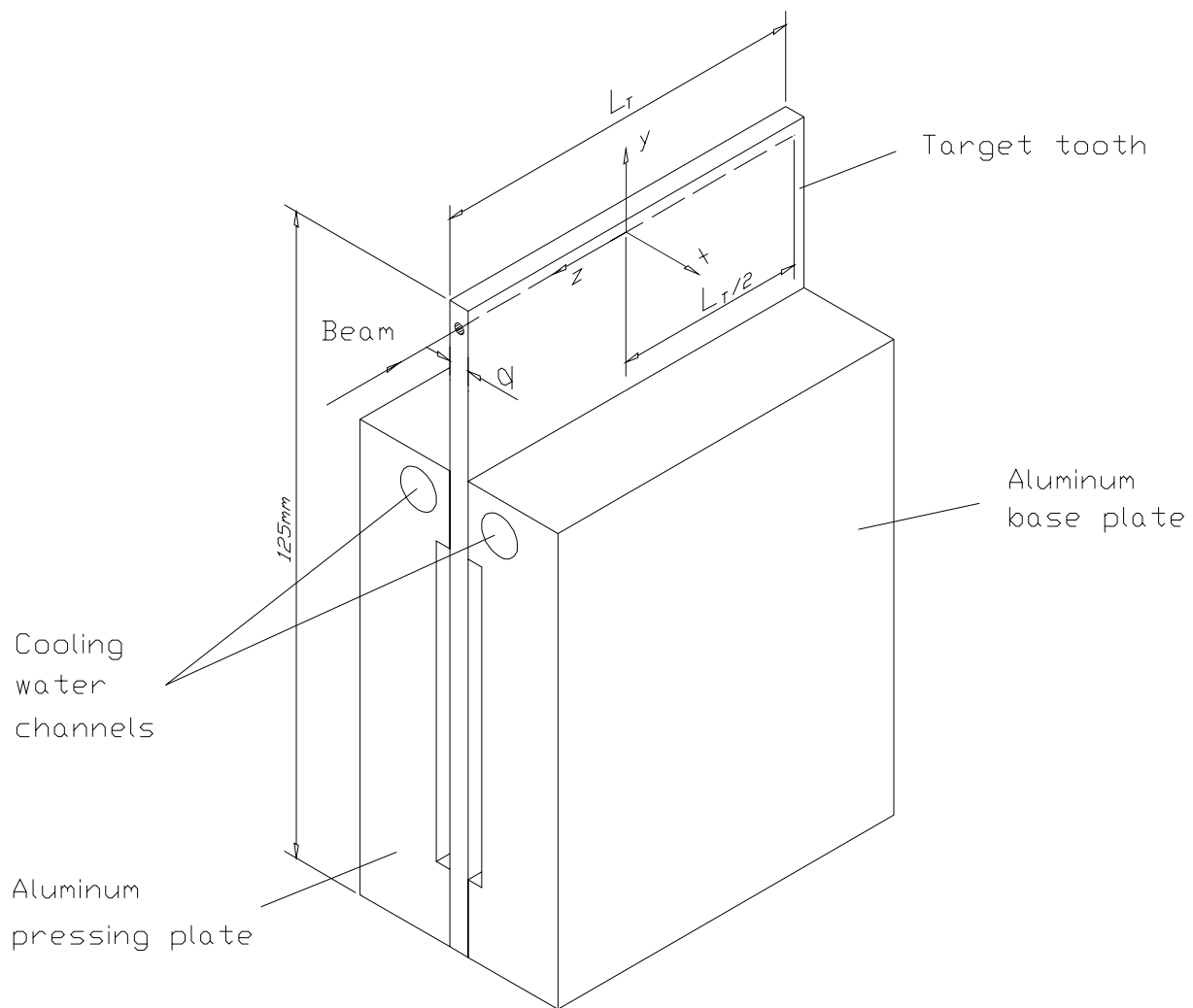


Figure 1.4: Model of the target tooth.

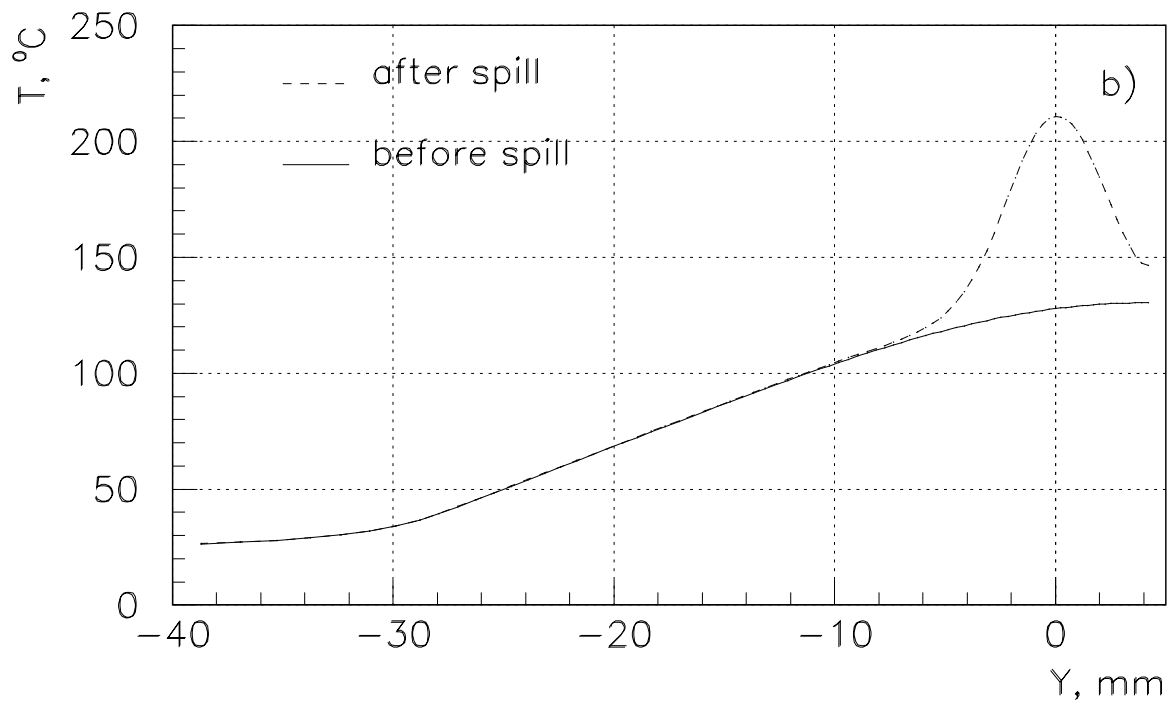
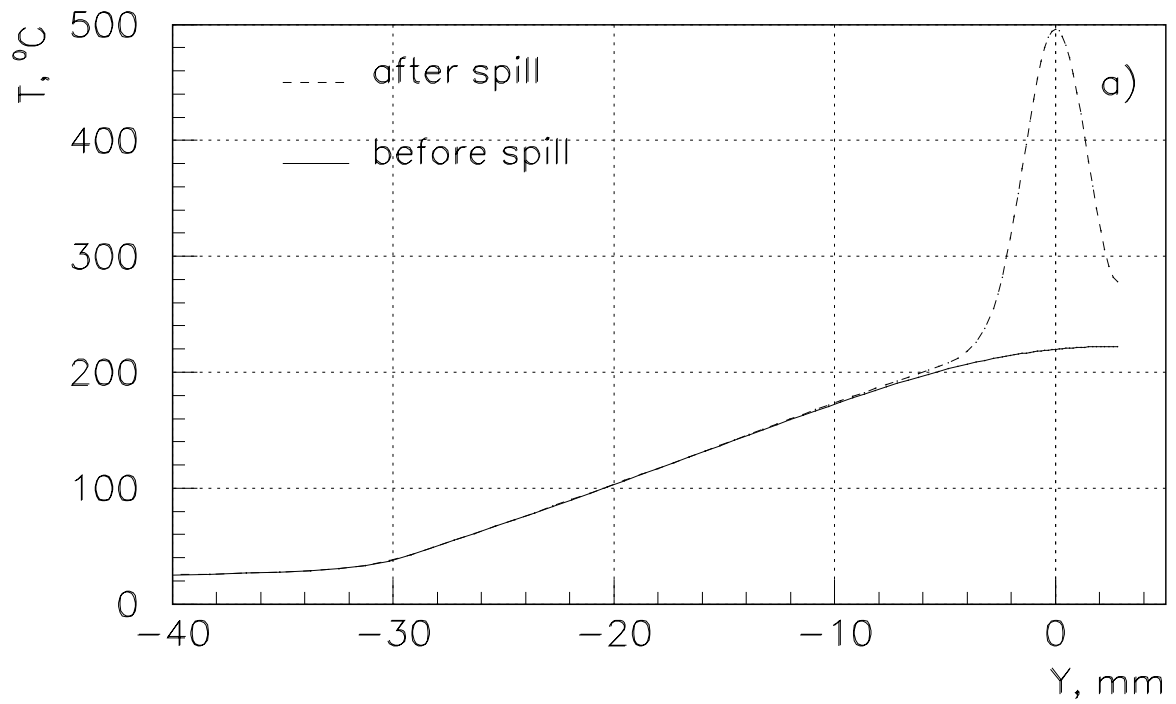


Figure 1.5: The temperature distributions in the target along the vertical axis: a) graphite target; b) beryllium target.

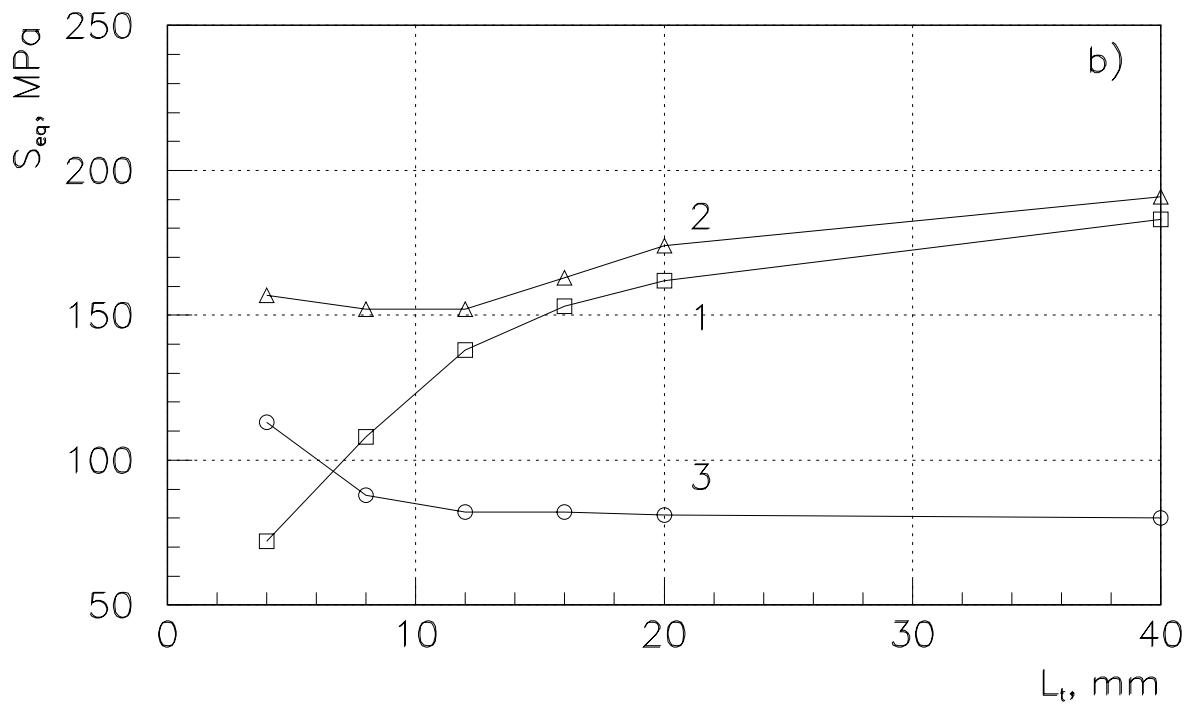
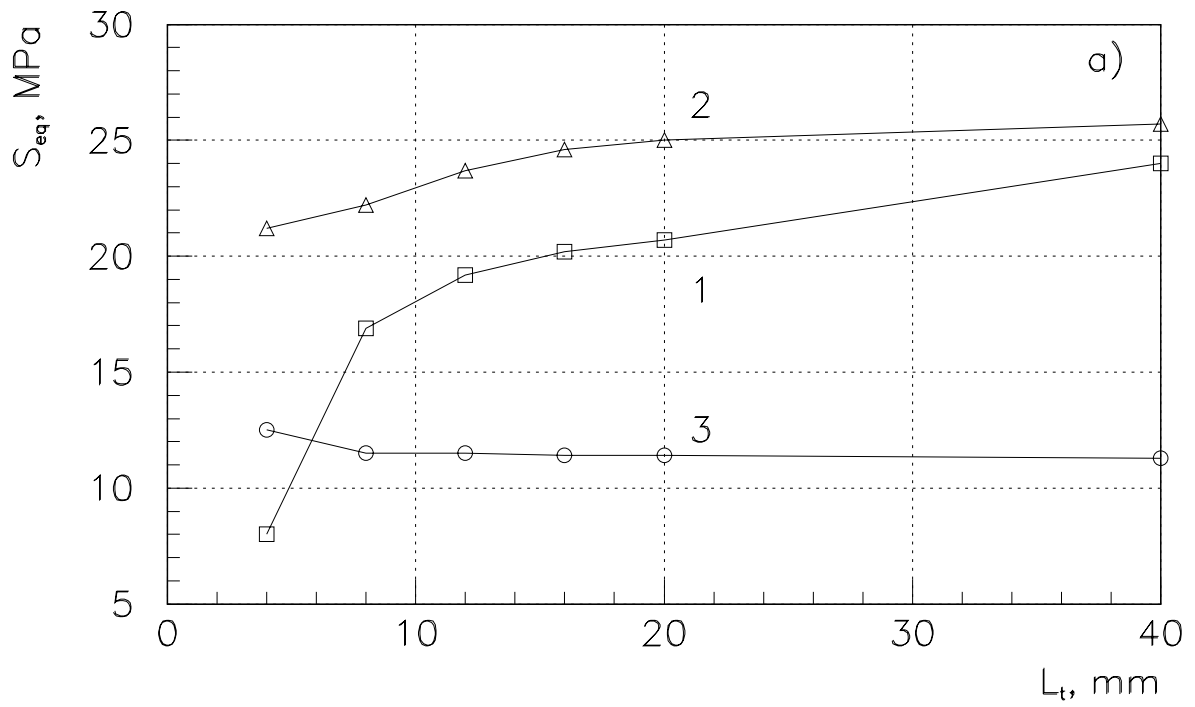


Figure 1.6: Equivalent stresses in different critical points of the target tooth as functions of the tooth length: a) graphite target; b) beryllium target.

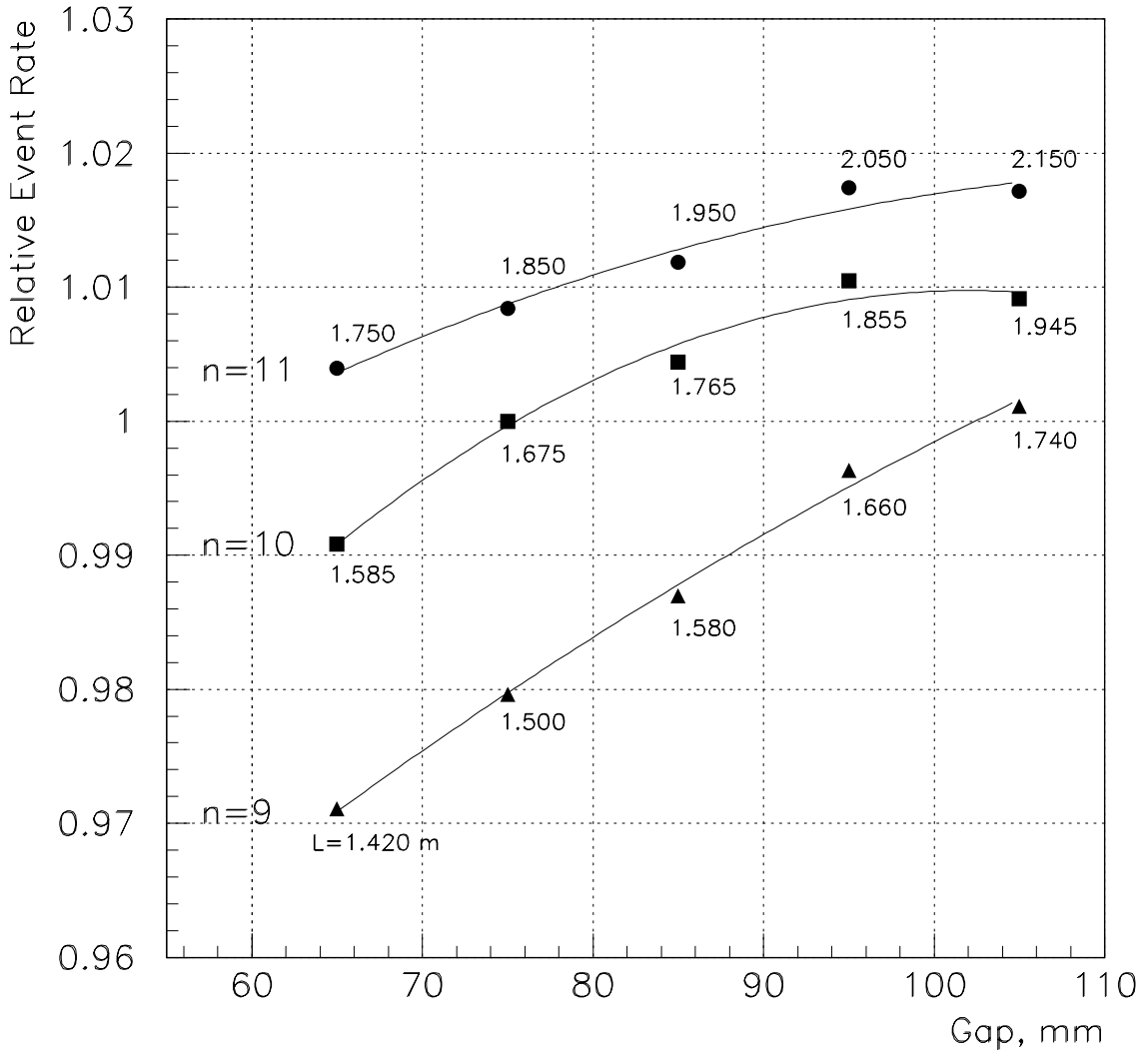
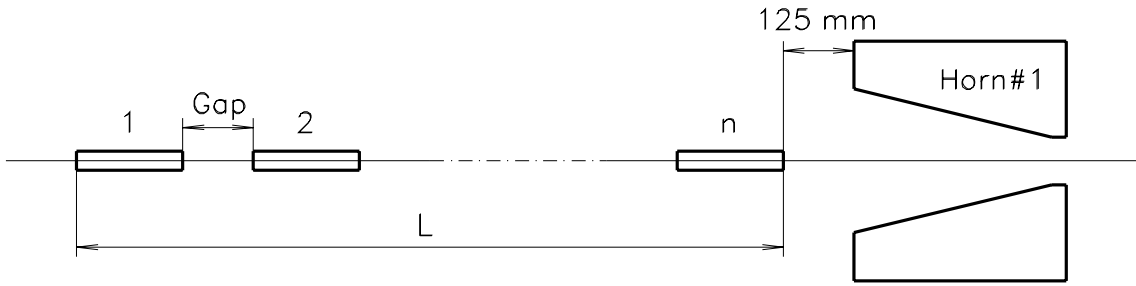


Figure 1.7: Target efficiency as function of number of segments and the gap between them.

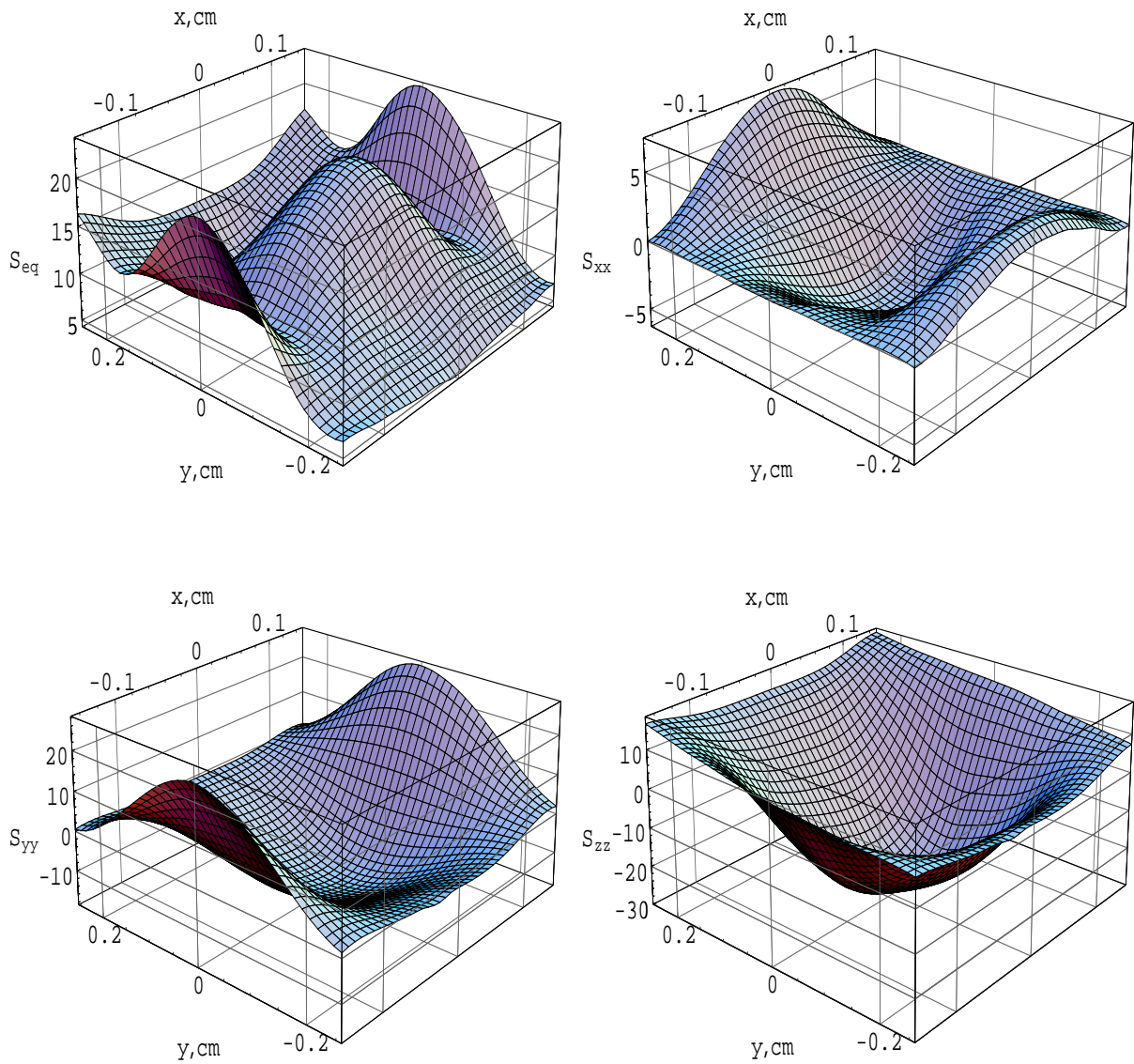


Figure 1.8: Stresses in the middle cross-section ($z = 0$) of the graphite target tooth.

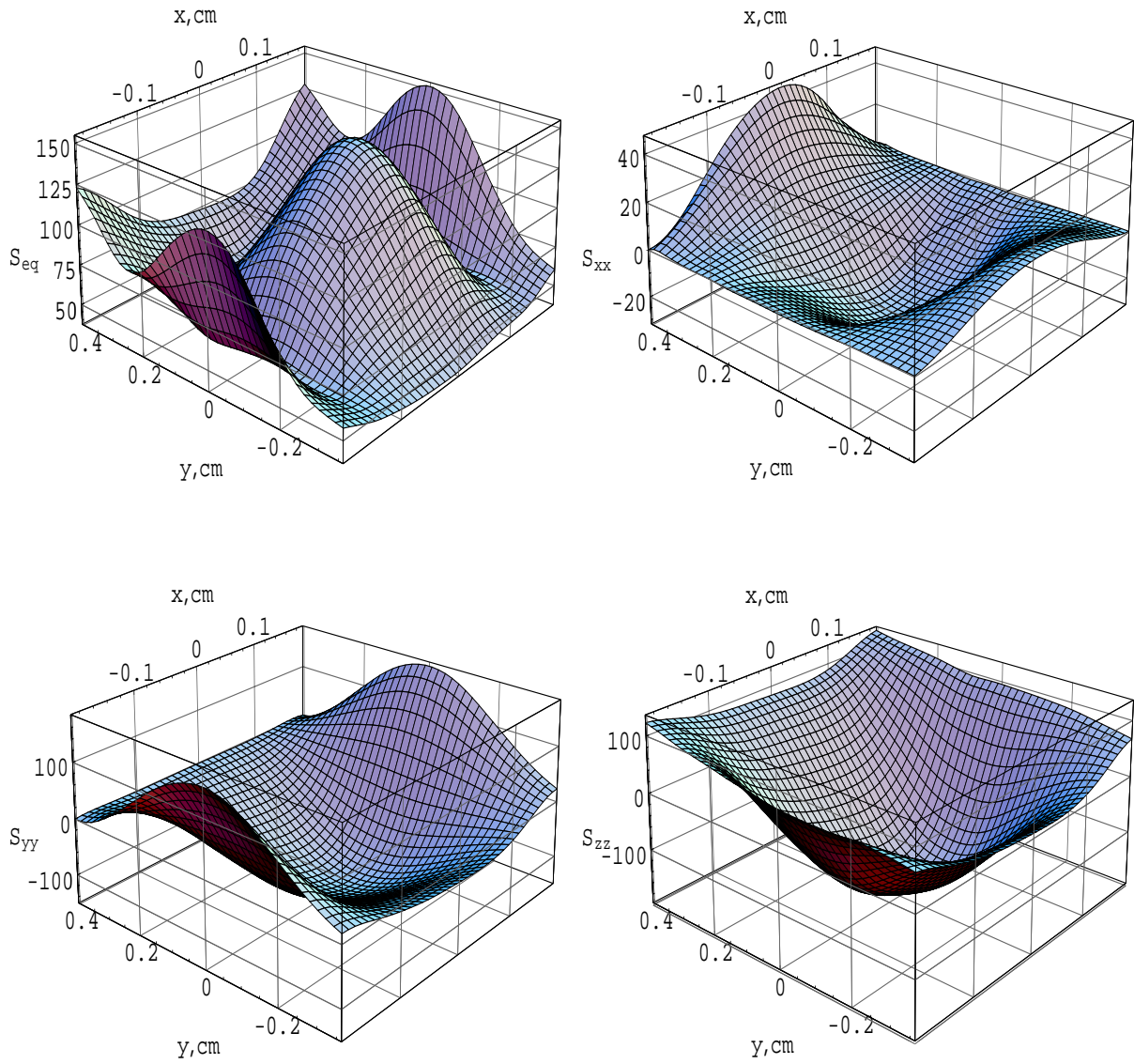


Figure 1.9: Stresses in the middle cross-section ($z = 0$) of the beryllium target tooth.

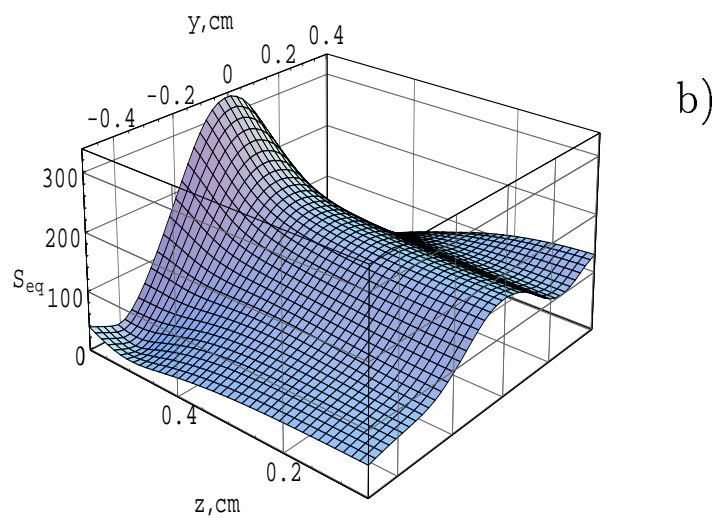
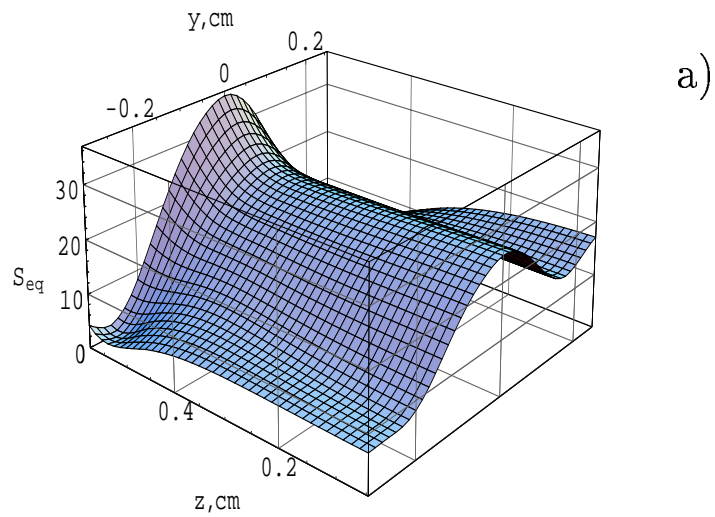


Figure 1.10: Distributions of an equivalent stress in YZ-plane for $x = d/2$: a) graphite target; b) beryllium target.

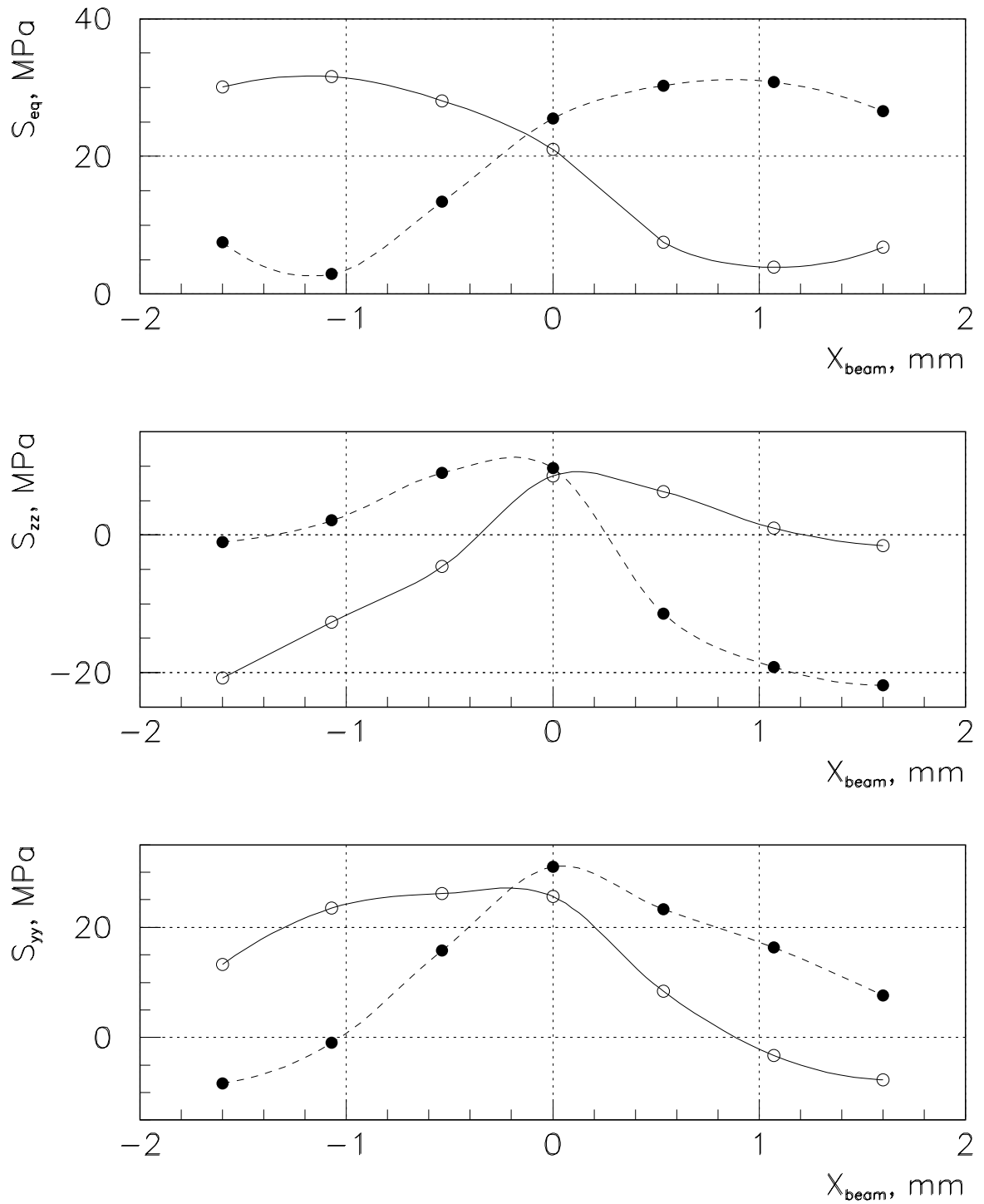


Figure 1.11: Stresses in the graphite target as functions of a beam location in X-direction: solid lines correspond to the point $(-d/2; 0; 0)$, dashed lines correspond to the point $(+d/2; 0; 0)$.

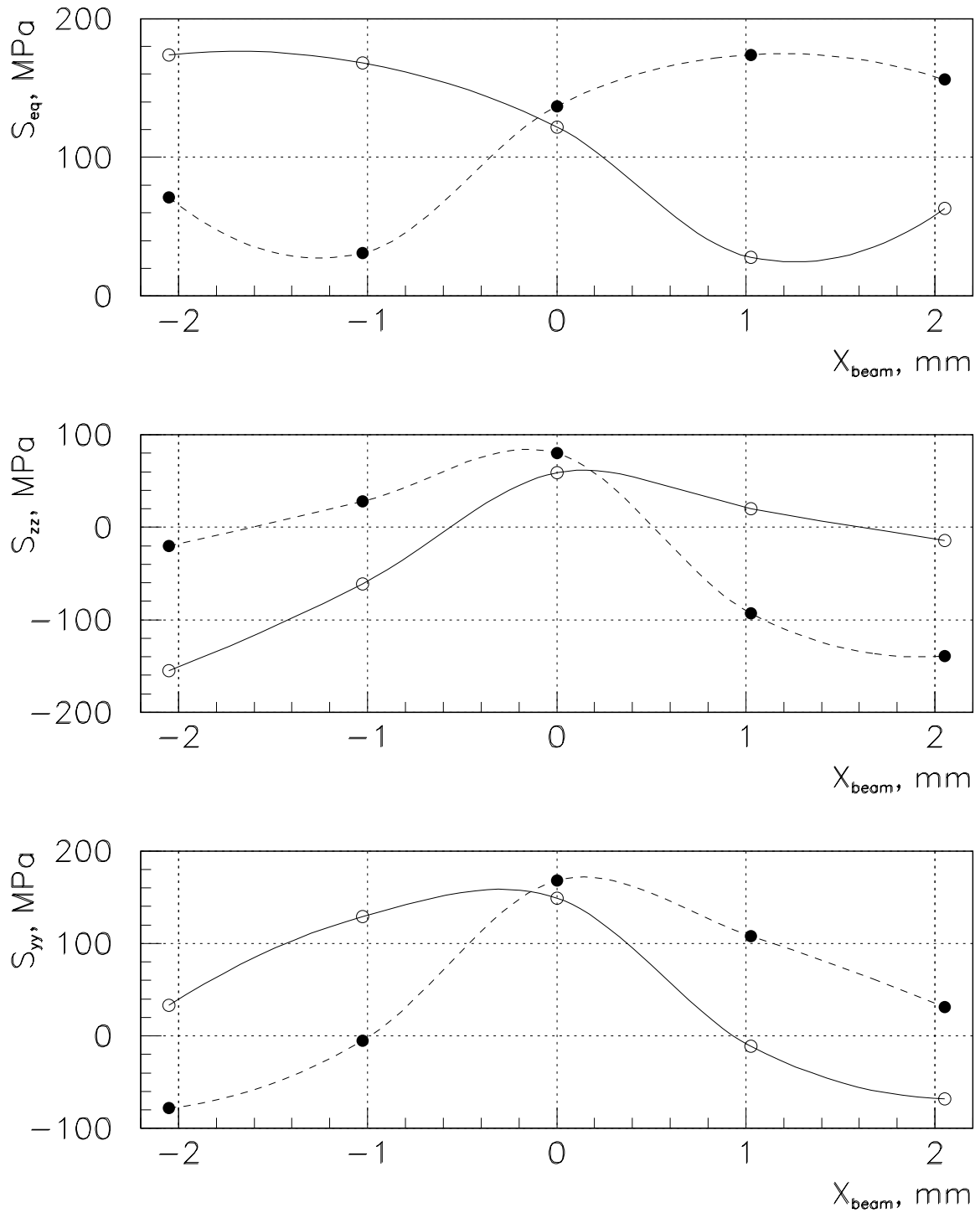


Figure 1.12: Stresses in the beryllium target as functions of a beam location in X-direction: solid lines correspond to the point $(-d/2; 0; 0)$, dashed lines correspond to the point $(+d/2; 0; 0)$.

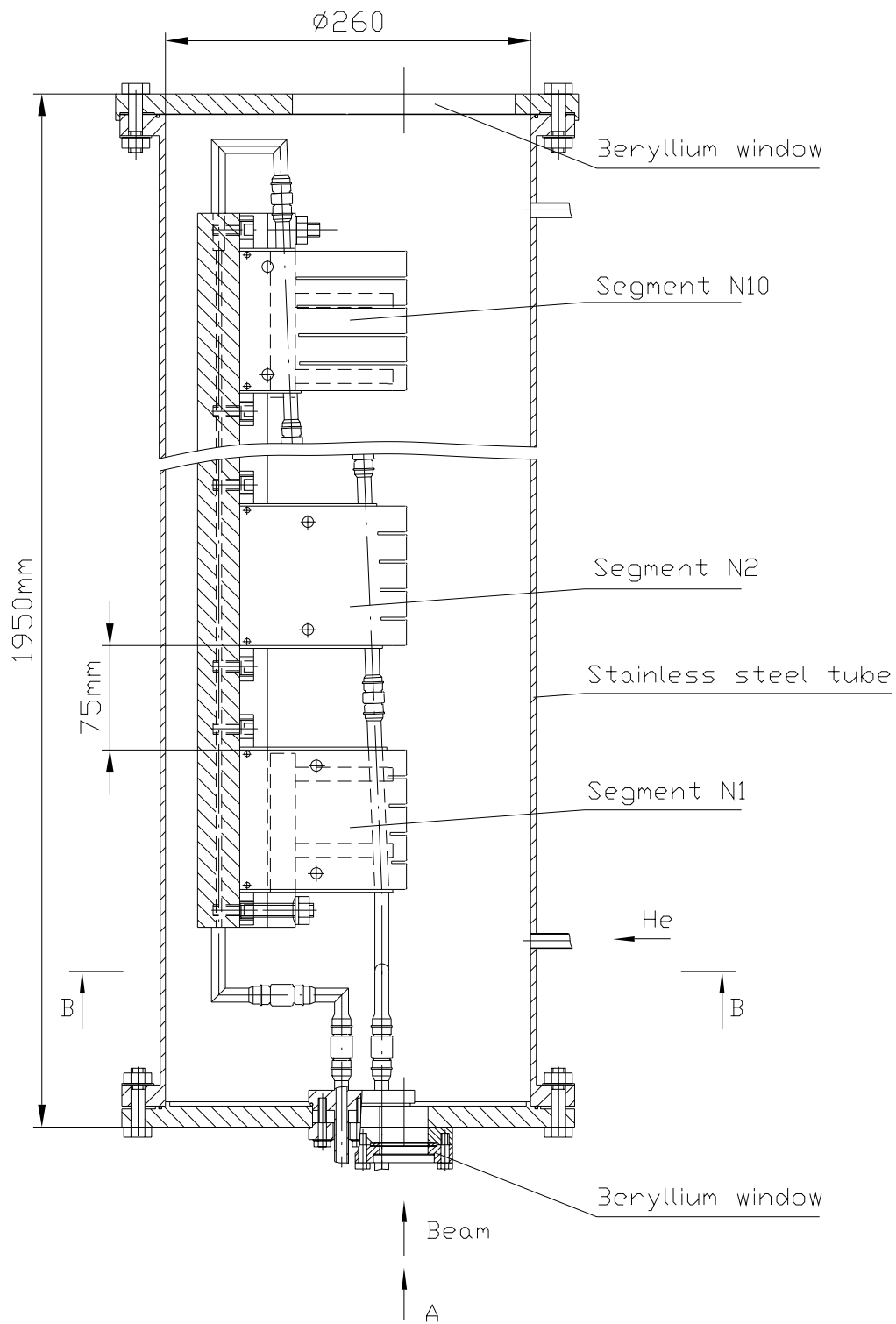


Figure 1.13: Schematical drawing of the full scale target.

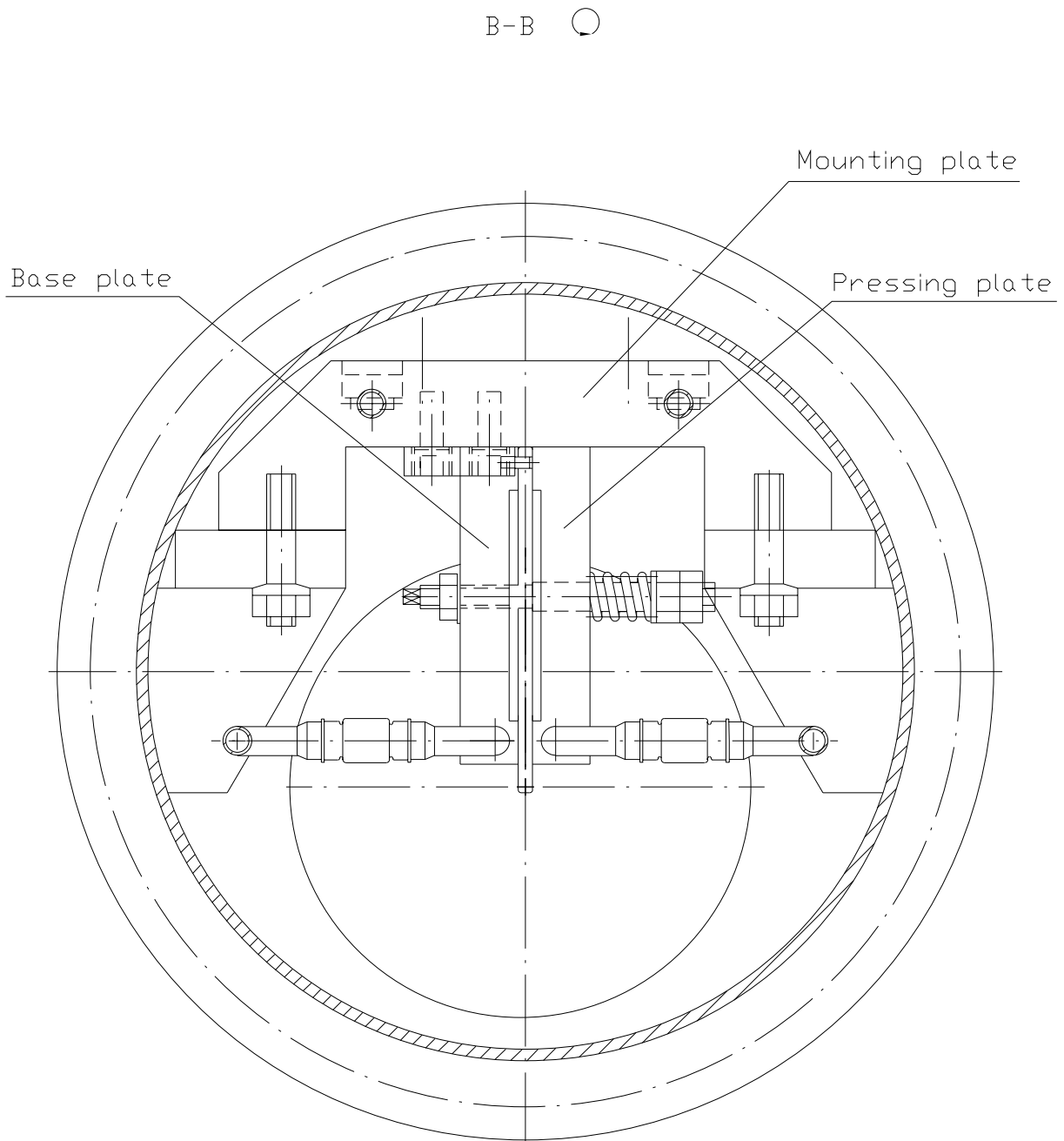


Figure 1.14: View B-B of the full scale target design (see Figure 1.13).

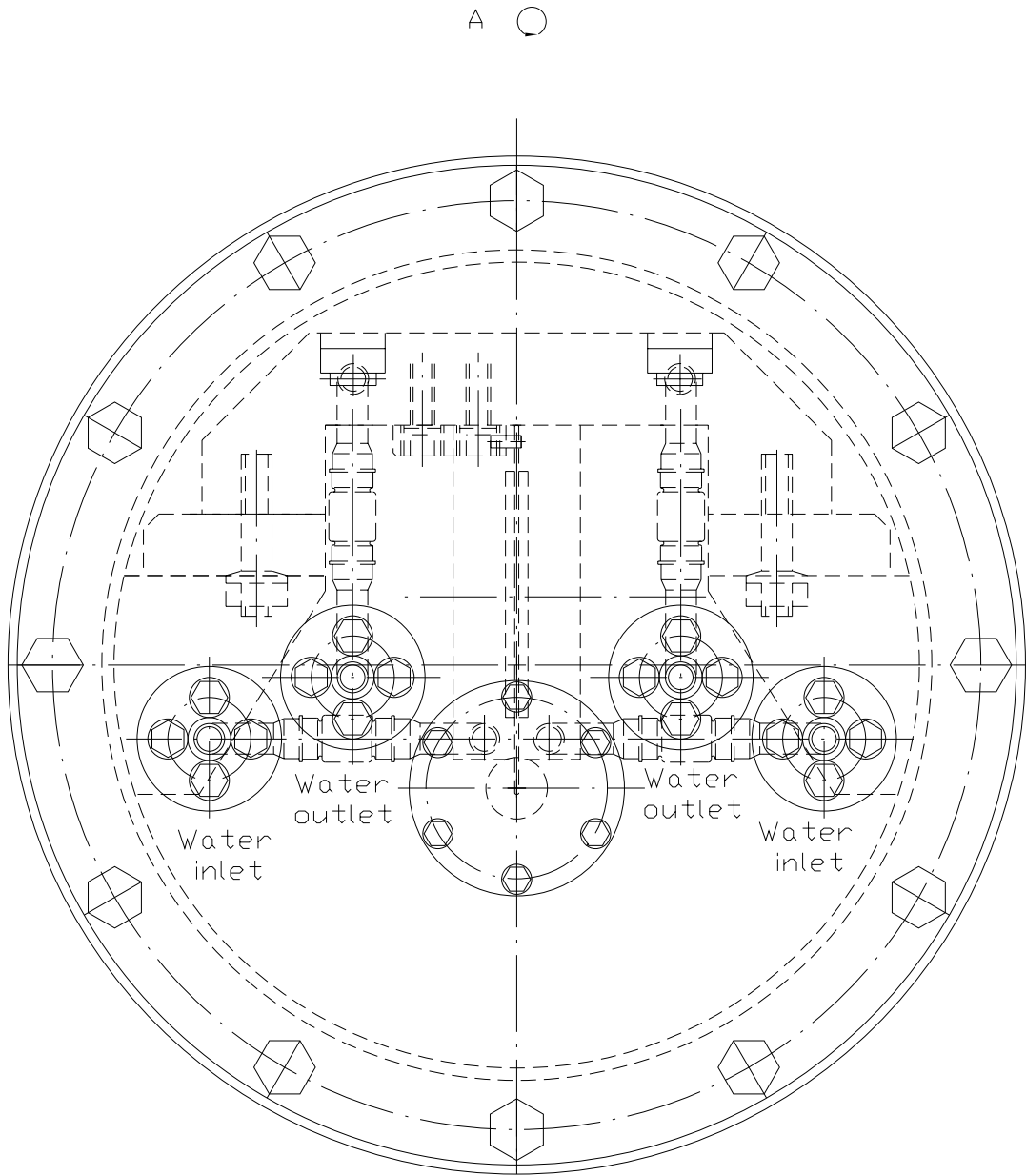


Figure 1.15: View A of the full scale target design (see Figure 1.13).

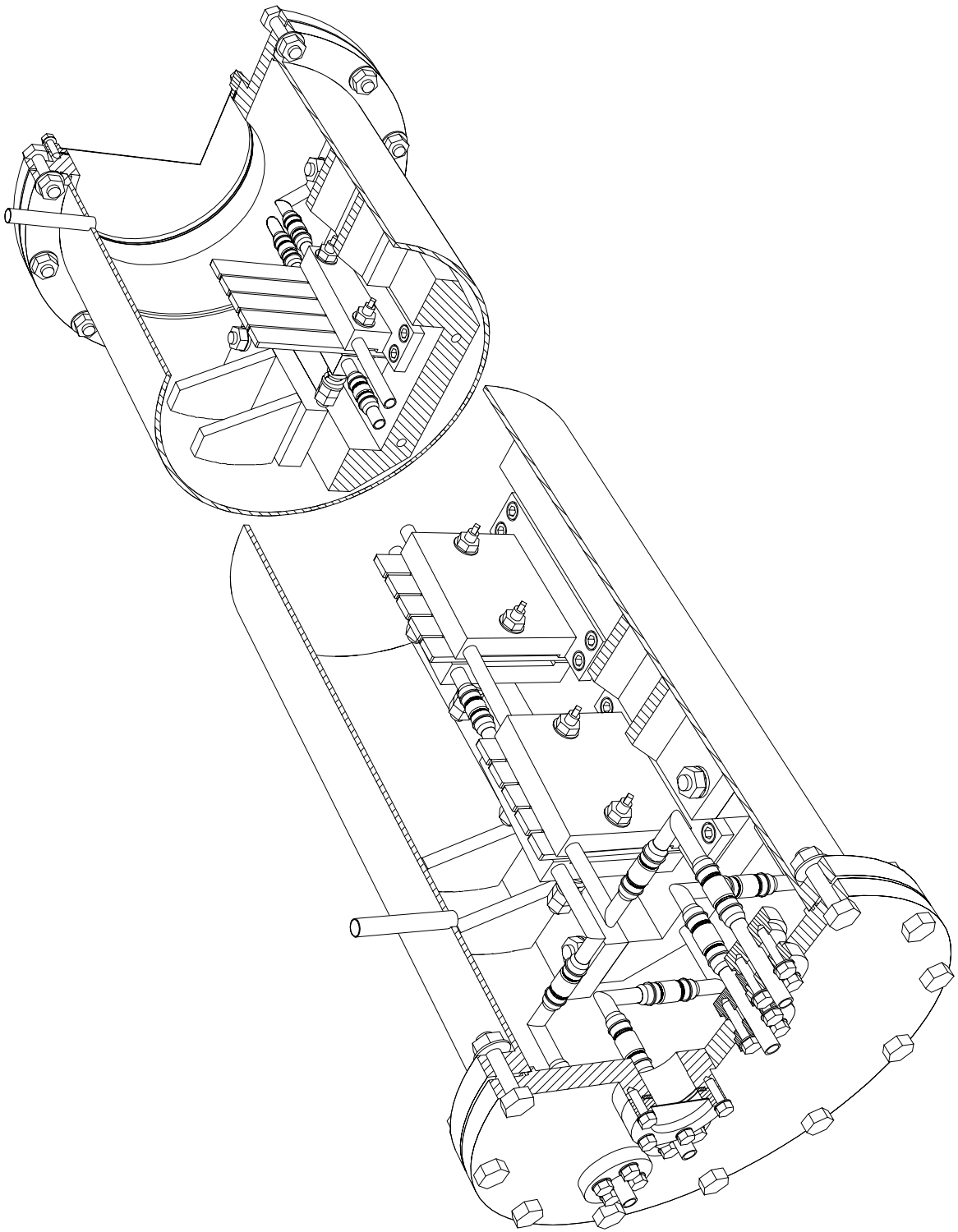


Figure 1.16: Perspective view of the target design.

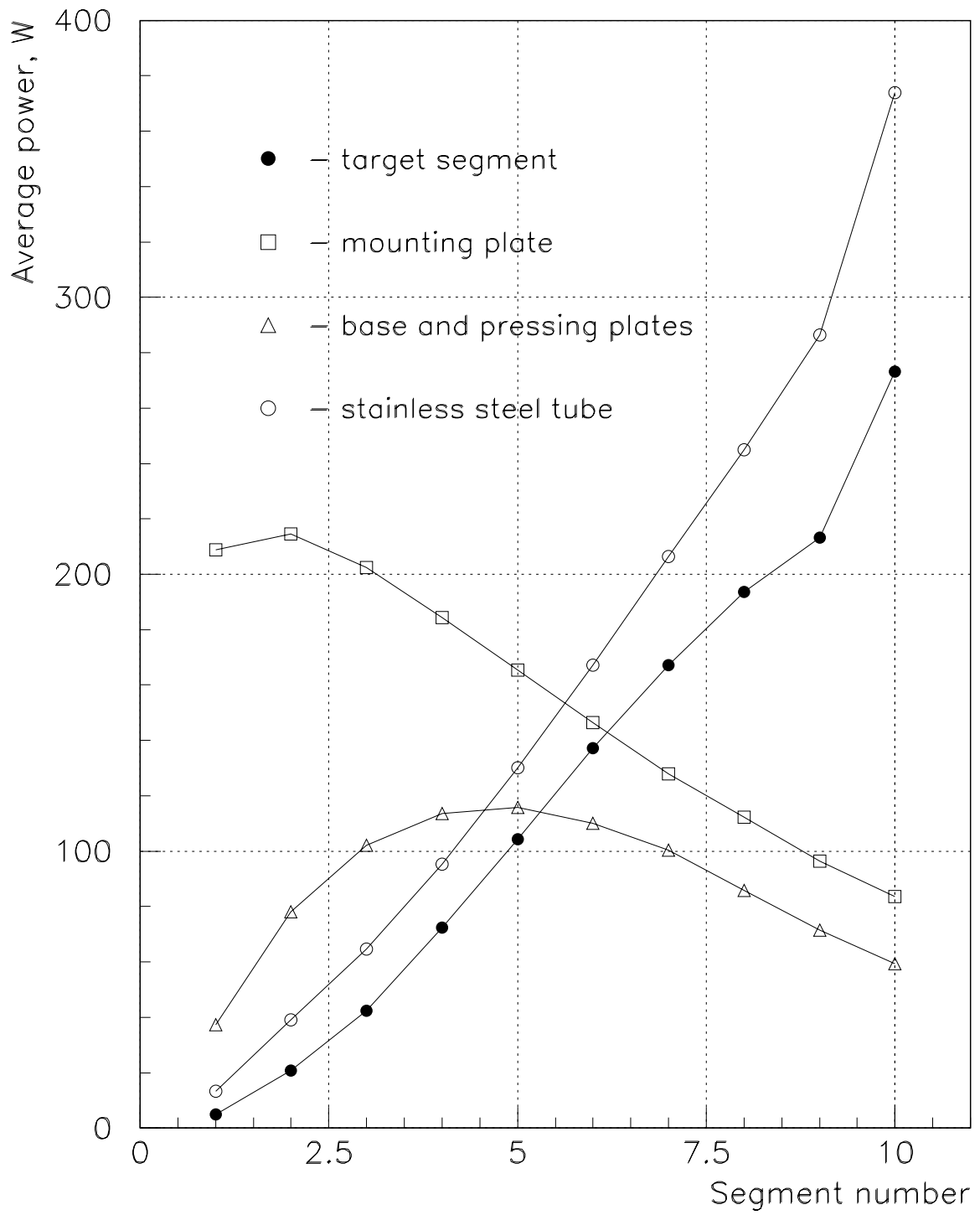


Figure 1.17: Average power deposited in different units of the target design as function of a segment number.

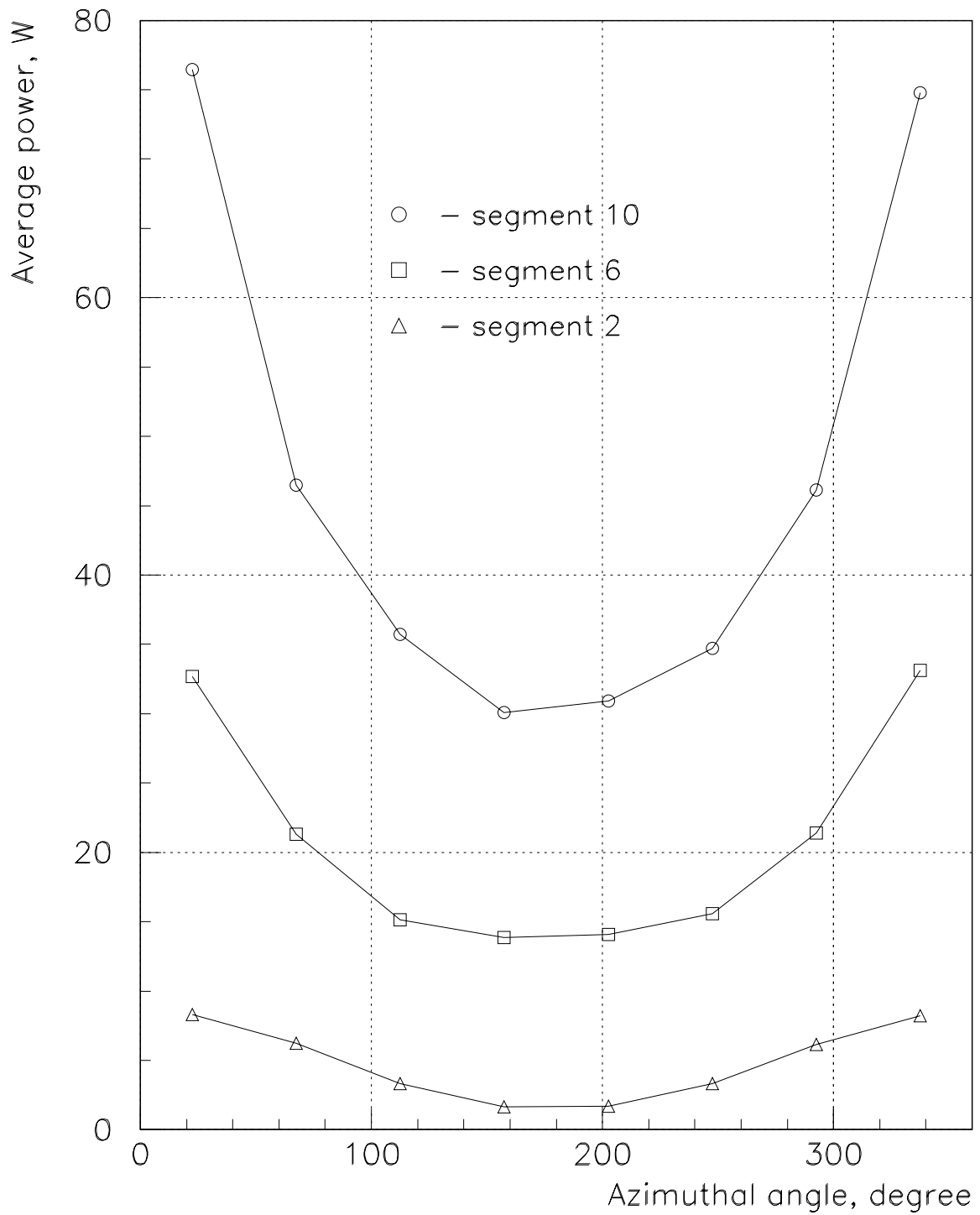


Figure 1.18: Azimuthal distributions of an average deposited power in the external tube for different number of a target segment. The angle is counted clock-wise from the vertical plane.

2 Target prototypes

Prototypes of the targets should reflect the main peculiarities of the full scale graphite and beryllium water cooled targets. It means that prototypes, if possible, should have:

- the same temperature distributions;
- the same thermal stresses (or the same safety factor);
- water cooling system and support design;
- Budal monitor for a beam monitoring.

In addition, the prototype design should have the special glass window to look at the target surface after testing.

2.1 General Description of the Target Prototype Design

The general view of the target prototype design is shown in Figures 2.1 and 2.2. Conventionally, the thickness of a target piece is equal to 4 mm in order to see it well at the small scale sketch. A target piece consisting of two identical parts is pressed between an aluminum base plate and an aluminum pressing plate (Figure 2.2). The vertical position of each part of the target is fixed by two small steel cylindrical pins with insulation layer made by the phosphatizing method. The base plate is clamped to the rigid stainless steel flange with four screws. Cooling water passes through the holes with inside diameter of 8 mm bored in the base and pressing plates.

Each of aluminum details are anodized by alumina ($30\mu\text{m}$ thick) in order to provide insulation of the target fin for the "Budal" monitor. Some flexible bellows are used in order to simplify the assembly of the target unit and to protect the base and pressing plates from any forces arose in a design. The special connection made by technology used in the similar transition in hot zones of nuclear reactors [12] provides the transition from aluminum to stainless steel piping. The quality of aluminum welding as well as transition will be tested by the X-ray detection.

The location of the testing beam is monitored by means of four nickel plates with thermocouples (see view D, Figure 2.3) and Split Foil Monitor (SFM, see Figure 2.4) which are mounted on the base plate. The temperature of the target tooth is measured by thermocouples placed in 9 mm

aside from the beam center (view C–C, Figure 2.3). For temperature measurements as well as for the beam position nickel plates the thermocouples of type J (Iron–constantan) [16] are planned to be used. In order to avoid possible thermal e.m.f. at the dissimilar material junction the special feedthrough with iron and constantan pins will be used [16]. For connections from the "Budal" monitor and SFM the feedthrough with glass insulation and kovar pins is specified. Electrical assembly will be made of a twisted copper pair with polyimide insulation. For a relatively short testing run the glass and polyimide insulation should be acceptable in view of its radiation resistance.

The assembly should be made using vacuum hygiene. After assembly of all details mentioned above the tube with the welded stainless steel flange and the stainless steel cylindrical plate is bolted to the target flange with a pure aluminum gasket in order to provide the tight vacuum connection. There are two pipes in the stainless steel plate to supply the target unit by helium atmosphere or to connect the vacuum pump. The visual examination of the target piece after testing by the proton beam may be made through quartz glass window. Water cooling pipes as well as the whole assembly of the target prototype unit should be tested to the vacuum leakproofness. The perspective view of the target design is shown in Figure 2.5.

2.2 Operation Conditions of the Prototype Testing. Thickness of the Target Piece

The main difficulty in a target prototype design is substantially different operating conditions between the full scale target and prototypes testing (see Table 2.1). As it was shown in the preliminary design [17], for Gaussian distribution of the NuMI beam and the testing AP0 beam with intensity $0.5 \cdot 10^{13}$ p/spill, scaling of the full scale beryllium target to the prototype is reached by decreasing of the beam spot sizes, the thickness of the target piece and the size of the tooth. Similar scaling has been carried out for the graphite target and gave the same result. Optimal thickness and length of the tooth were 1.32 mm and ~ 3.0 mm for beryllium prototype and 1.0 mm and ~ 2.5 mm for graphite one respectively. Such small thickness and length of prototype teeth will create serious problems in machining of the target and proper steering of the proton beam to the target.

Targets	Full scale	Prototypes
Type of the beam	NuMI beam	Test beam
Beam energy	120 GeV	120 GeV
Beam type	proton	proton
Beam distribution in X-direction	non-Gaussian	Gaussian
Beam distribution in Y-direction	\sim Gaussian	Gaussian
Number of particles per spill	$4.0 \cdot 10^{13}$	$(0.5-1.0) \cdot 10^{13}$
Total kinetic energy	0.768 MJ	$(0.096-0.192)$ MJ
Pulse duration	1.0 ms	$8 \mu\text{s}$
Repetition period	1.9 s	1.5 s

Table 2.1: Operating conditions of targets.

But in practice the NuMI beam has non-Gaussian distribution and is essentially non-symmetrical in X-direction (horizontal). On the other hand the intensity of the testing beam may vary from $0.5 \cdot 10^{13}$ to $1.0 \cdot 10^{13}$ p/spill and necessary temperature jump due to the beam heating of the target piece in this range of intensities may be reached only by varying of the beam spot sizes if the thickness of the target piece is fixed. By these reasons the full scale target scaling to the prototype can not be full for stress distributions and may be reached only in terms of temperature jumps and maximal equivalent stresses. So, the piece of the target prototype may have larger thickness than mentioned above and necessary temperature jump and equivalent stress should be provided by varying of beam spot sizes for different values of intensities of the testing beam and length of the target tooth. It is convenient to take 1.78 mm (0.07") thick graphite sheet because Poco Graphite supplies precision thin sheets with such thickness. For beryllium prototype the thickness of the target was taken 2.29 mm (0.09").

2.3 Beam Spot Sizes for Prototypes Testing

Estimations of sizes of the testing beam and the target prototype have been carried out for beryllium target to work out the criterion of similarity. The number of particles per spill in the testing beam is eight times less than in the NuMI beam. So, in order to provide the same deposited energy density in a prototype as in the full scale target, the density of protons in

first approach should be 8 times increased. For the beryllium fin target, operating with the proton beam spot size $\sigma_x = 1.0$ mm and $\sigma_y = 2.0$ mm, the maximum deposited energy density is equal to 0.0312 GeV/g/p. It means that for the test beam the maximum deposited energy should be about 0.250 GeV/g/p.

Maximum deposited energy densities near the beam axis in the beryllium cylindrical target as function of the proton beam spot size (data received by computer code MARS [9]) are listed in Table 2.2. As it follows from Table 2.2 the test beam spot size should be of $\sigma = (0.4-0.5)$ mm.

$\sigma_x = \sigma_y$, mm	ΔE , GeV/g/p
1.0	0.057
0.9	0.070
0.8	0.080
0.7	0.110
0.5	0.210
0.4	0.320
0.3	0.540

Table 2.2: Deposited energy densities in Be-target.

MARS simulations for the beryllium fin target with $\sigma_y \approx 2\sigma_x$ show that the deposited energy density of 0.250 GeV/g/p is reached at sizes of the test beam $\sigma_x = 0.34$ mm, $\sigma_y = 0.68$ mm for intensity $0.5 \cdot 10^{13}$ p/spill and $\sigma_x = 0.49$ mm, $\sigma_y = 0.98$ mm for intensity $1.0 \cdot 10^{13}$ p/spill. For the testing beam with such sizes in front of the target, the beam axis should be settled in ~ 2.2 mm aside from the upper end of the target. Such estimations for graphite prototype testing give following values of the beam spot size: $\sigma_x = \sigma_y = 0.3$ mm and 0.4 mm for $0.5 \cdot 10^{13}$ and $1.0 \cdot 10^{13}$ p/spill respectively. The beam axis should be settled in ~ 1.0 mm aside from the upper end of the target.

2.4 Temperature and Quasistatic Thermal Stress Considerations

Temperature and quasistatic thermal stresses have been computed by the program HAST [10] using distributions of deposited energy densities received by MARS [9] for sizes of the target prototype and the testing beam mentioned above.

HAST calculations show that to realize the maximum temperature of a prototype target the same as in the full scale target ($T_{\max} = 219^{\circ}\text{C}$ and $T_{\max} = 508^{\circ}\text{C}$ at heat transfer coefficient to water equal to $10\text{ kW/m}^2/\text{K}$) is practically impossible due to a very low power ($\sim (30\text{--}60)\text{ W}$), absorbed in a prototype. In the full scale target the absorbed power in the second segment is approximately equal to 214 W .

Temperature calculations of the prototype were made using the following boundary conditions:

- the heat transfer coefficient (HTC) to water is equal to $2.5\text{ kW/m}^2/\text{K}$. Such HTC corresponds to the cooling water velocity equal to 0.41 m/s and the total water flow rate of 2.46 l/min ;
- the thermoresistance between the target piece and the aluminum base and pressing plates is equal to zero;
- the ambient temperature is equal to 20°C ;
- the radiation is taking into account for the coefficient of blackness equal to one;
- the HTC to an ambient atmosphere (α_a) is equal to $10\text{ W/m}^2/\text{K}$. Calculations show that $\alpha_a = (0\text{--}10)\text{ W/m}^2/\text{K}$ practically does not influence on the target piece temperature. Decreasing of a HTC leads to a very high temperature constant of a target.

The target prototype under cooling conditions, mentioned above, reaches the steady state in about $(40\text{--}50)$ pulses. The temperature distribution in the beryllium target along the vertical axis before and after spill in the steady state is shown in Figure 2.6a (point $x = y = 0$ corresponds to the proton beam axis, the beam intensity is equal to $1.0 \cdot 10^{13}$). The comparison of calculations of analogous distributions for the graphite prototype made by HAST and ANSYS is shown in Figure 2.6b. One can see that both computer codes give same results of the temperature in the graphite target prototype.

Each segment of the target is cut several times in a vertical direction into subsegments (teeth) in order to minimize the quasi-static thermal stresses in the target. Equivalent stresses in different critical points of the target tooth (see Figure 1.4): 1 – $(0;0;0)$, 2 – $(+d/2;0;0)$ and 3 – $(0;0;\pm L_t/2)$ as

functions of the tooth length are shown in Figures 2.7 (beryllium) and 2.8 (graphite). As one can see from Figure 2.7, for the tooth length equal to 6 mm the maximal stresses for testing intensities $0.5 \cdot 10^{13}$ and $1.0 \cdot 10^{13}$ p/spill are equal to 150 and 152 MPa respectively. For graphite prototype with length of the tooth equal to 8 mm the maximal stresses for intensities mentioned above are equal to 27 and 32 MPa respectively.

It is interesting to compare results of ANSYS (2D approach, $S_{zz}=0$) and HAST (3D) calculations of transverse stresses. Such comparison is shown in Figure 2.9 in terms of behavior of S_{xx} and S_{yy} along the X-axis at $y = z = 0$ for the graphite target tooth (beam intensity $1.0 \cdot 10^{13}$ p/spill). As follows from these plots, the results received by both computer codes agree well. Besides it confirms that rounding of the tooth corner does not influence on stresses in most crucial points $(\pm d/2; 0; 0)$.

The comparison between the temperature and strength characteristics of full scale targets and target prototypes are summarized in Table 2.3.

Target	Graphite			Beryllium		
	Full scale	Prototype		Full scale	Prototype	
Subsegment length, mm	18.4	8.0		12.6	6.0	
Thickness, mm	3.2	1.78		4.1	2.29	
Beam intensity, ppp	$4 \cdot 10^{13}$	$5 \cdot 10^{12}$	$1 \cdot 10^{13}$	$4 \cdot 10^{13}$	$5 \cdot 10^{12}$	$1 \cdot 10^{13}$
Beam size, $\sigma_x \times \sigma_y$, mm ²	0.67×1.28	0.30×0.30	0.40×0.40	0.88×2.00	0.34×0.68	0.49×0.98
T_{\max} at steady state, °C	508	467	557	220	142	173
ΔT , °C	280	394	425	82	91	90
Maximal S_{eq} , MPa	25	27	32	152	152	150

Table 2.3: Comparison of different targets characteristics.

For steering of the testing beam on the target it is very important to know whether the target withstands the stresses arose in it when the beam is not centered with respect to the target. In order to investigate such situation some calculations of the beam deposition energy and stresses for various beam positions were made for the case of a steady state (the most crucial situation). Two-dimensional distributions of stresses in the tooth

when the beam is well centered in the target, i.e. the beam center-weight coincides with the center of the target are shown in Figure 2.10 for beryllium and Figure 2.11 for graphite. Equivalent stress distributions in YZ-plane for $x = d/2$ are shown in Figure 2.12a for beryllium target and in 2.12b for graphite one. As follows from Figure 2.12 there is the stress concentration at the corner ($x = \pm d/2, z = \pm L_t/2$). In order to avoid the stress concentration this corner should be rounded. Estimations show that for the radius of rounding equal to $d/2$, where d is the thickness of target fin, the stress concentration is vanished. This value of the radius of rounding was specified for the target manufacturing.

HAST calculations show, that in the case when the beam is centered off the most crucial situation arises in points $(\pm d/2; 0; 0)$. The results of stress calculation in these points as function of transverse coordinate X_{beam} of the beam center are shown in Figure 2.13 for beryllium prototype and in Figure 2.14 for graphite one. The maximal values of equivalent stresses reach 220 MPa in beryllium and 54.8 MPa in graphite targets. Taking into account that mis-steering of the beam will be continued for a short period of a time only, the targets will withstand such stresses.

2.5 Summary

The target prototype design described in this section was discussed several times with the FNAL staff. We would like to thank J.Hylen, K.Anderson, G.Waver for helpful discussions at various stages of the prototype design.

For the testing run it is useful to know stresses in targets as function of the beam spot size for different testing intensities. Such calculations will be done in July–September. The full set of the production drawings of prototypes will be supplied together with manufactured units in September.

Estimations show that for the graphite target prototype it is necessary to take into account dynamic stresses because the tooth sizes are compared with length of the sound propagation in $8 \mu\text{s}$. The attempt of such analysis will be made in July–September.

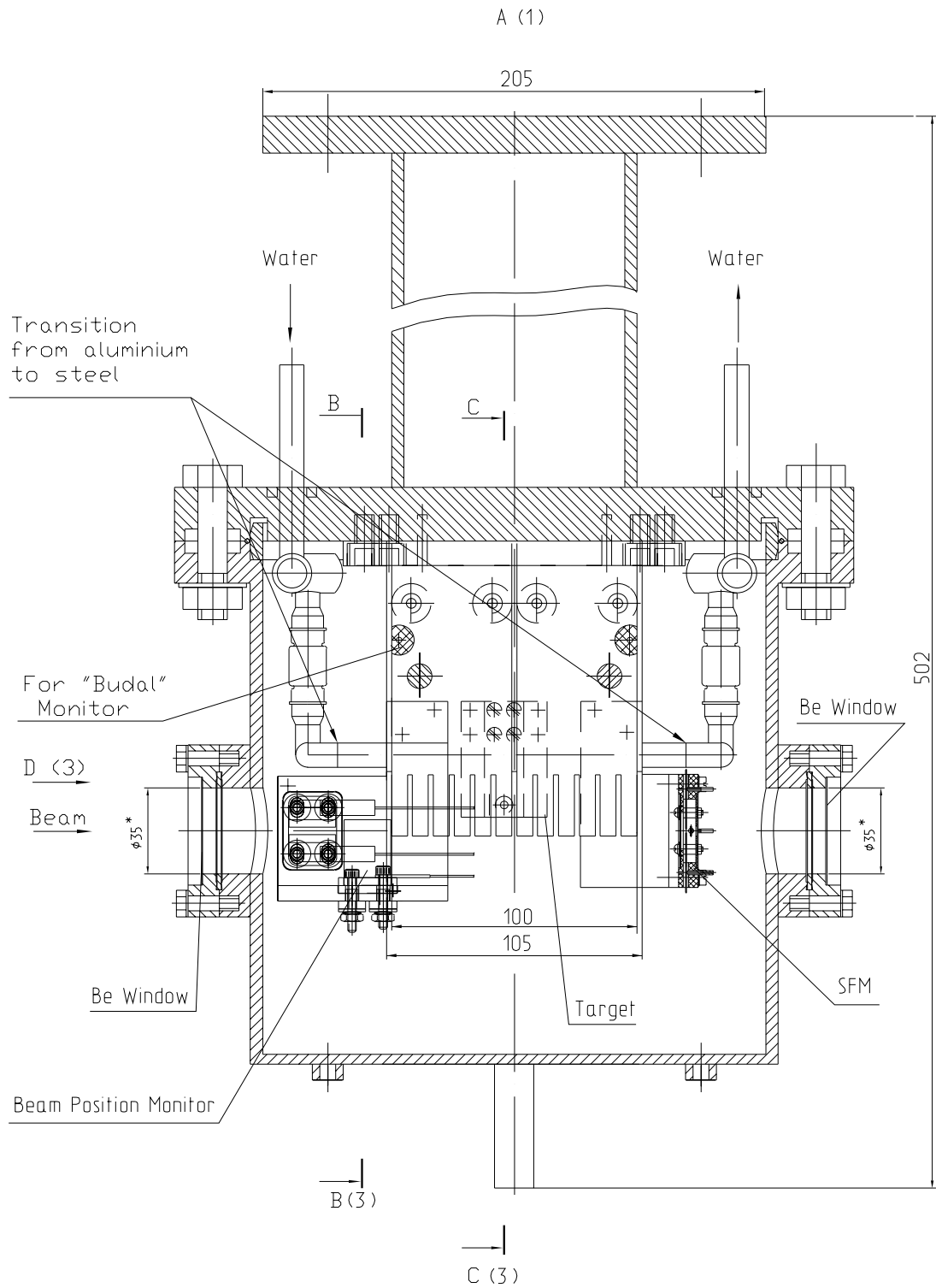


Figure 2.1: Cross-section of the target prototype design in the vertical plane along the beam axis.

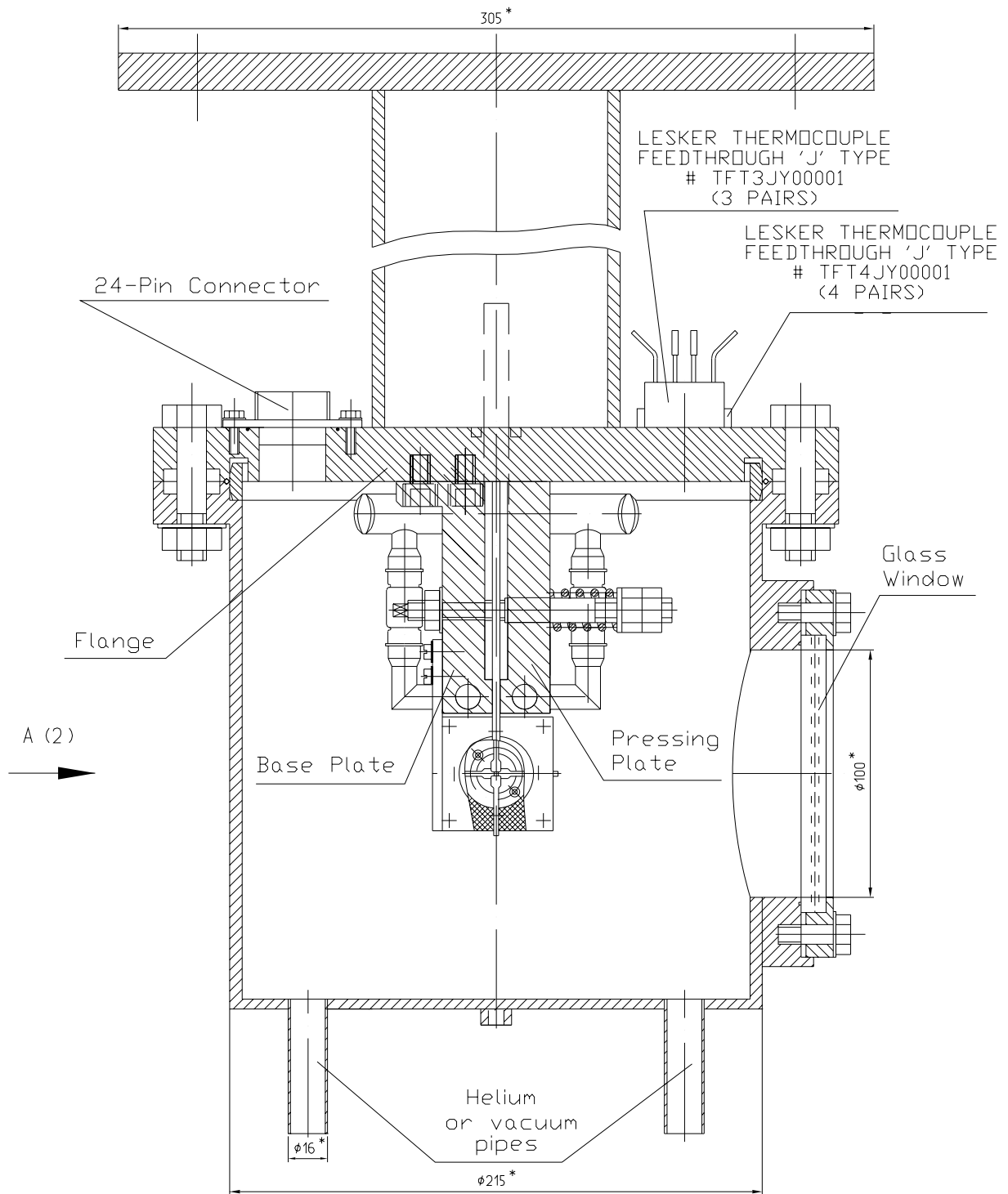


Figure 2.2: Transverse cross-section of the target prototype design.

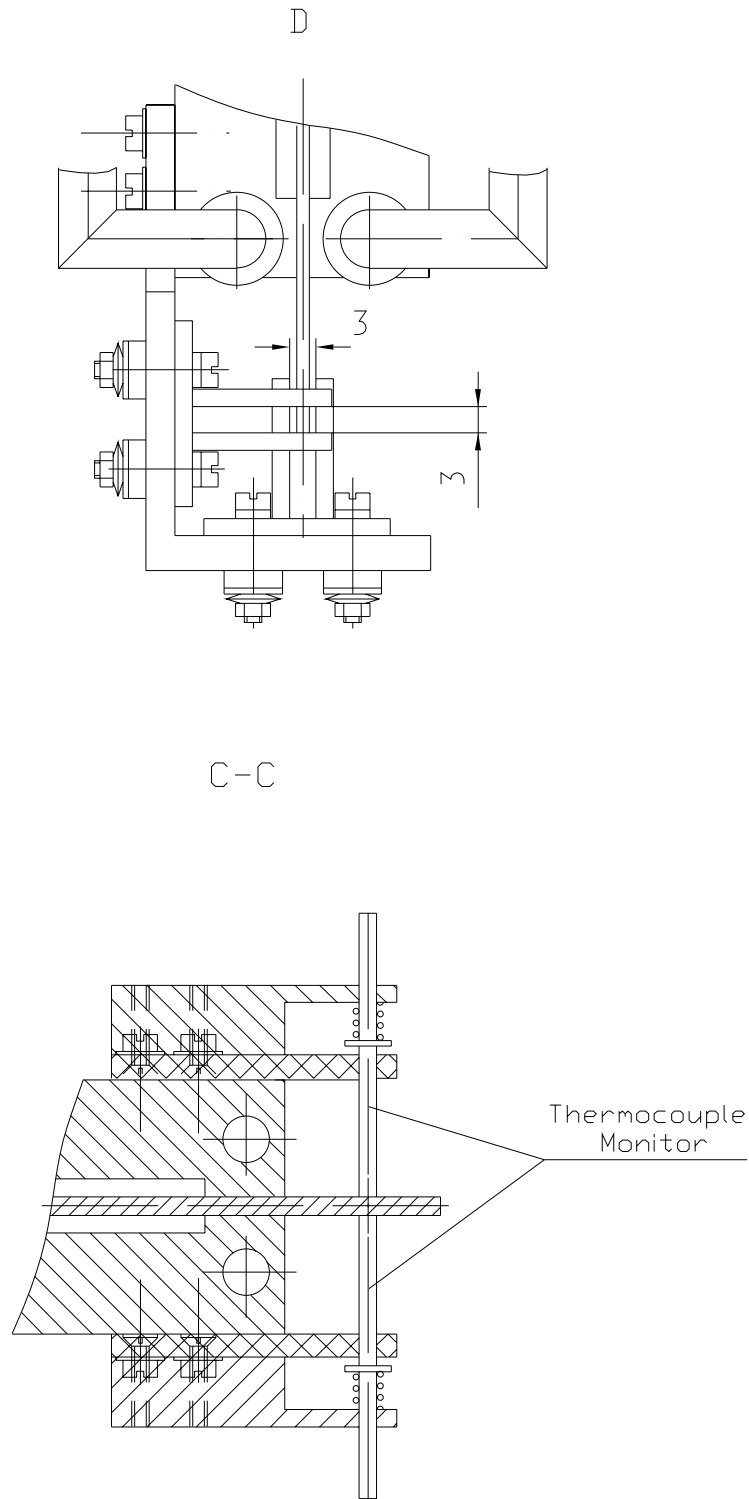


Figure 2.3: Nickel pads beam location indicator (view D) and system of temperature monitoring of the target (view C-C).

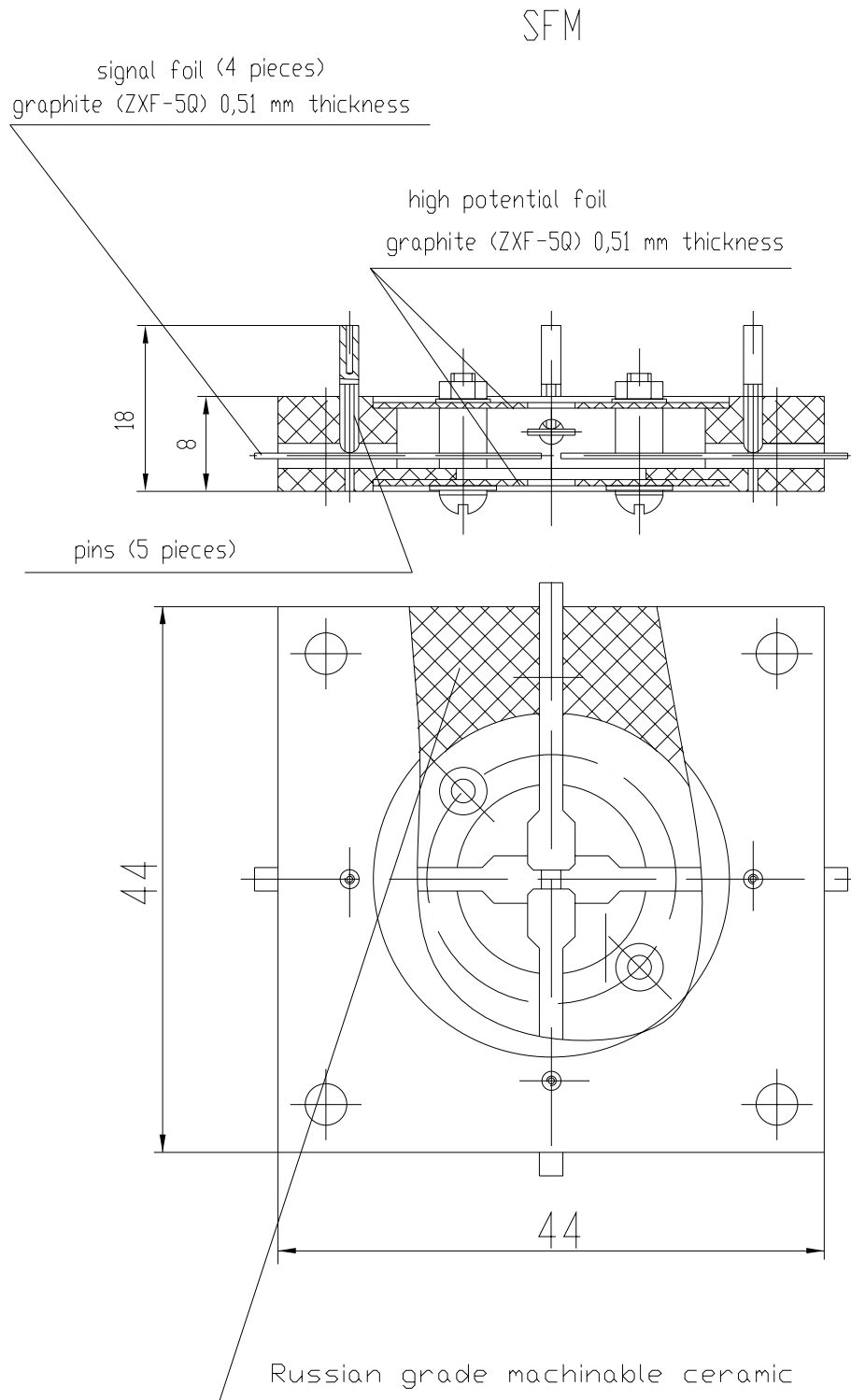


Figure 2.4: Split foil monitor.

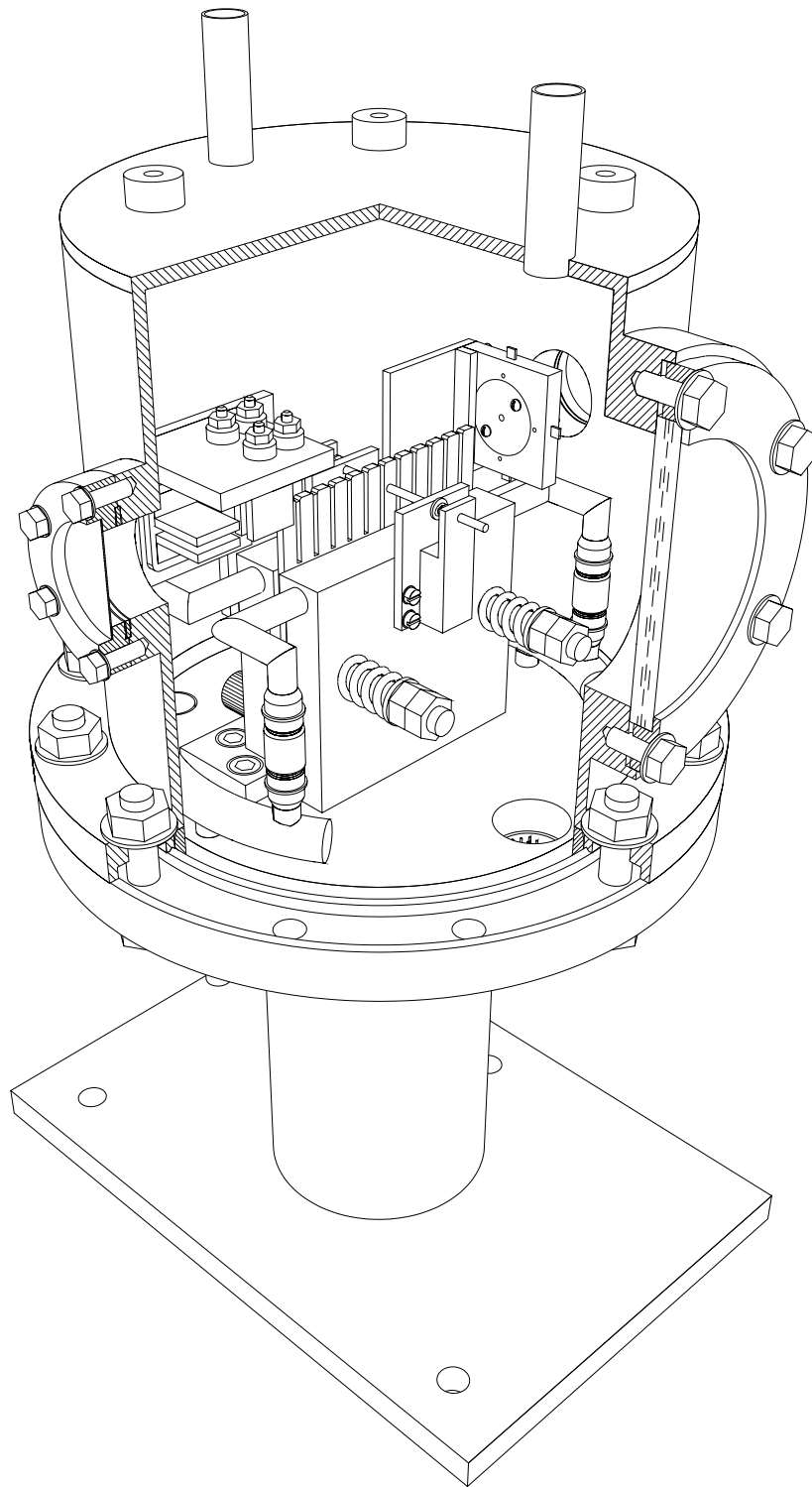


Figure 2.5: Perspective view of the target prototype design.

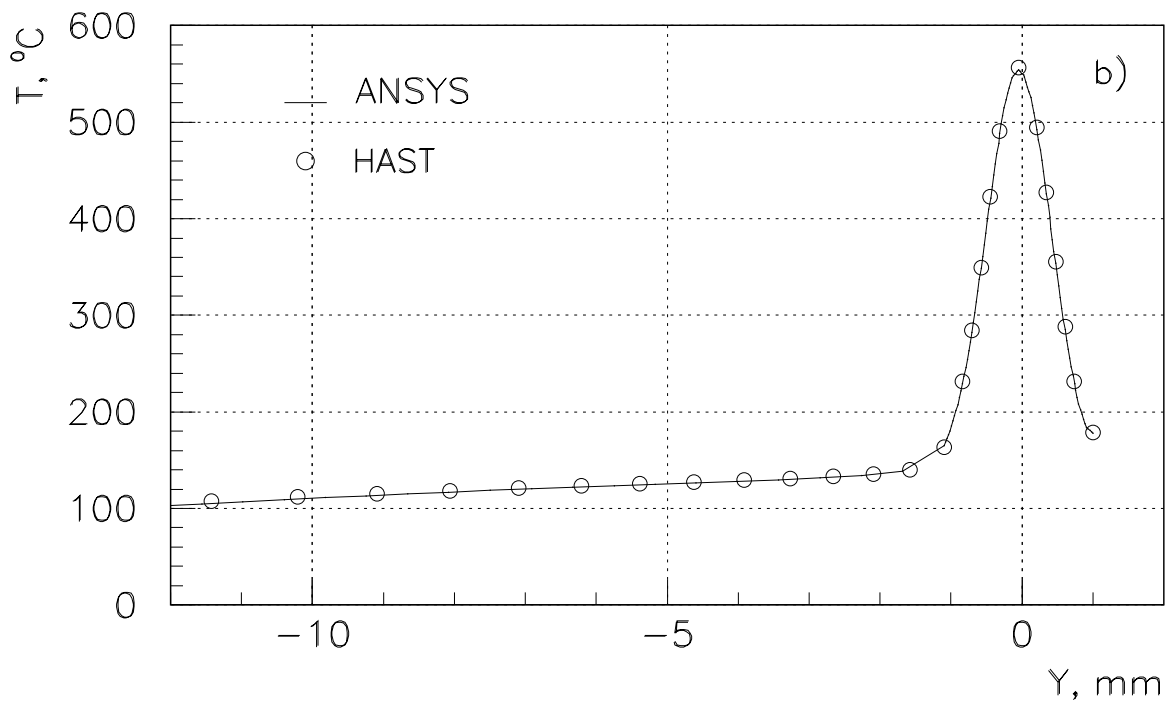
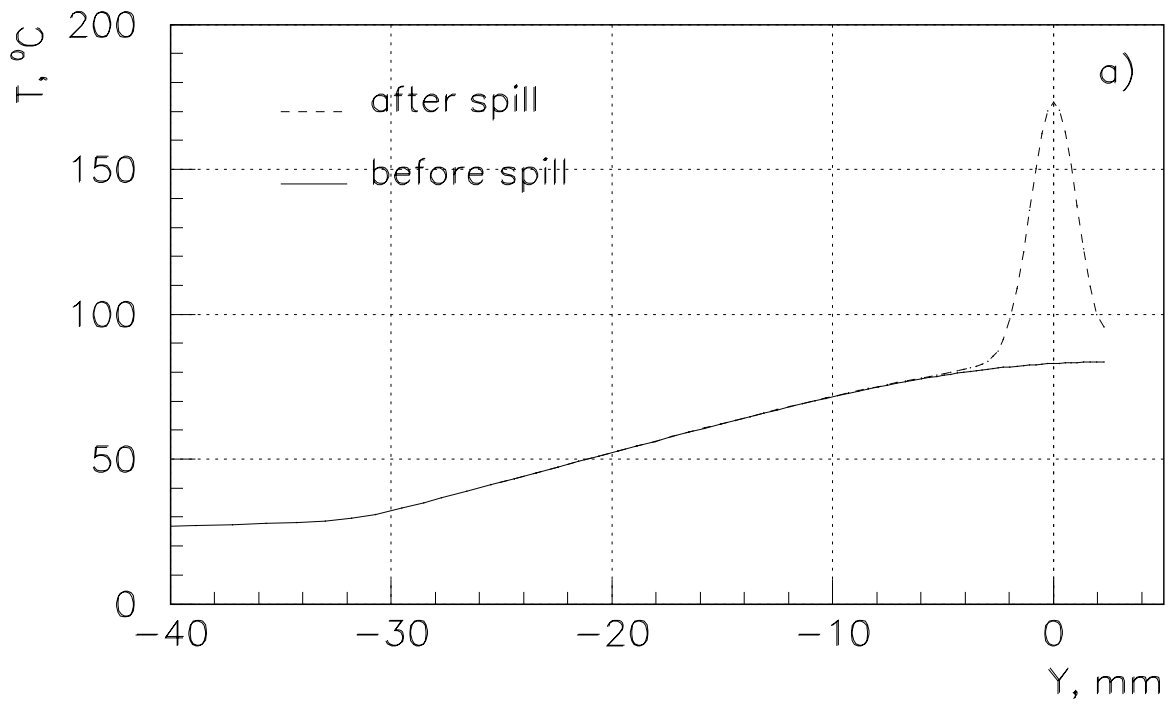


Figure 2.6: Temperature distributions at a steady state in the target prototype along the vertical axis ($1.0 \cdot 10^{13}$ p/spill): a) beryllium; b) graphite (ANSYS and HAST).

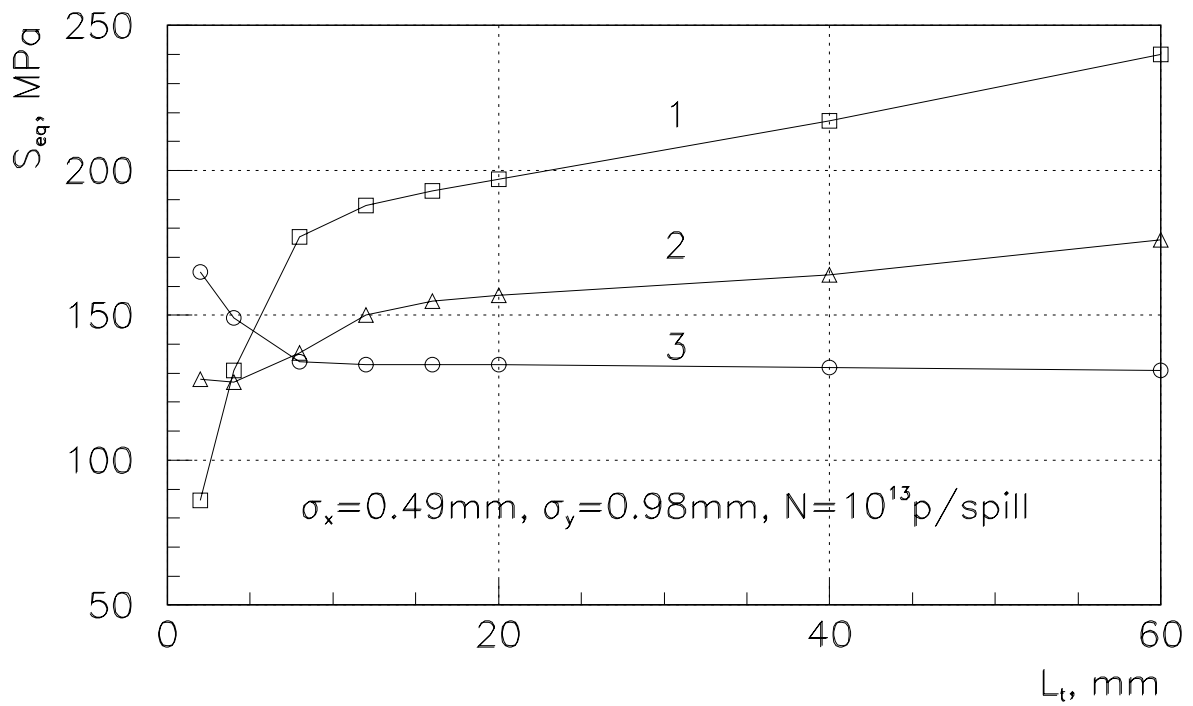
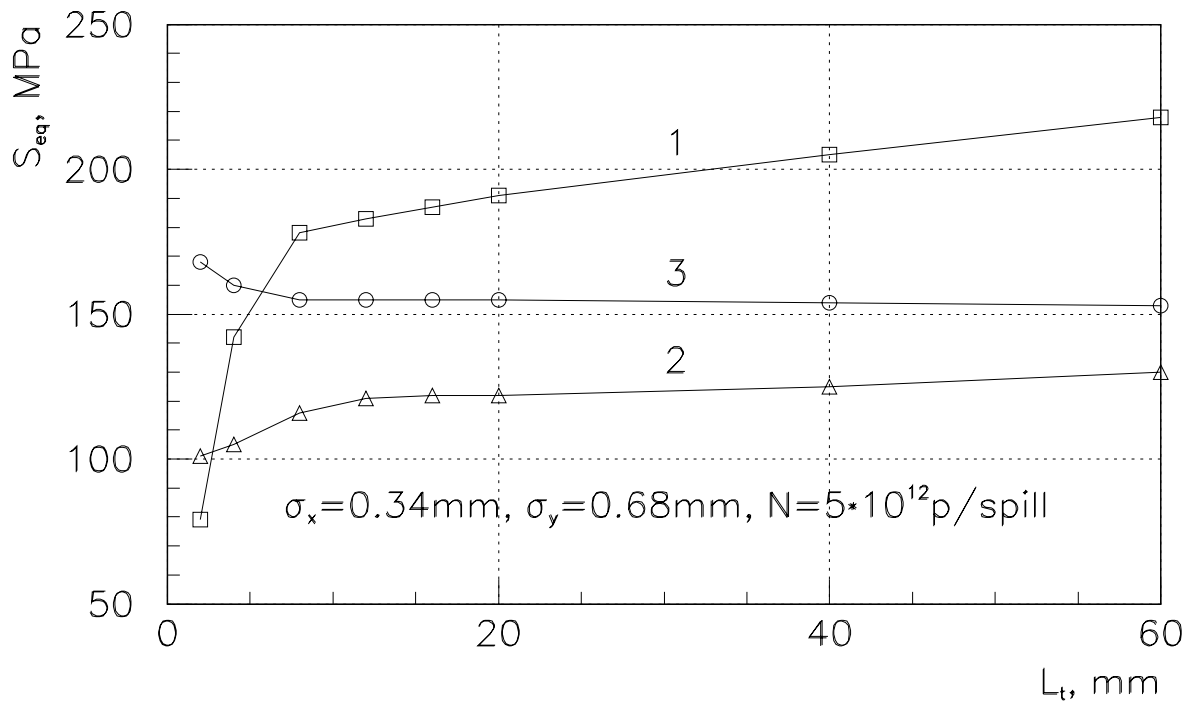


Figure 2.7: Equivalent stresses in different critical points of the target tooth in the beryllium prototype as functions of the tooth length.

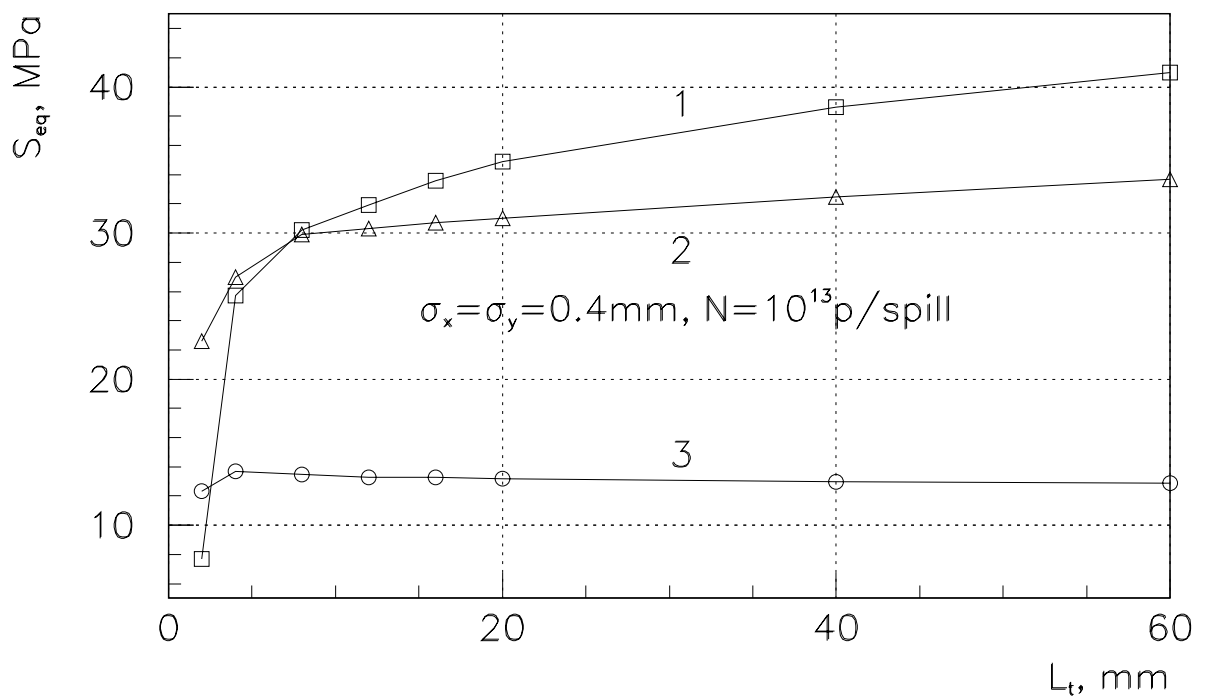
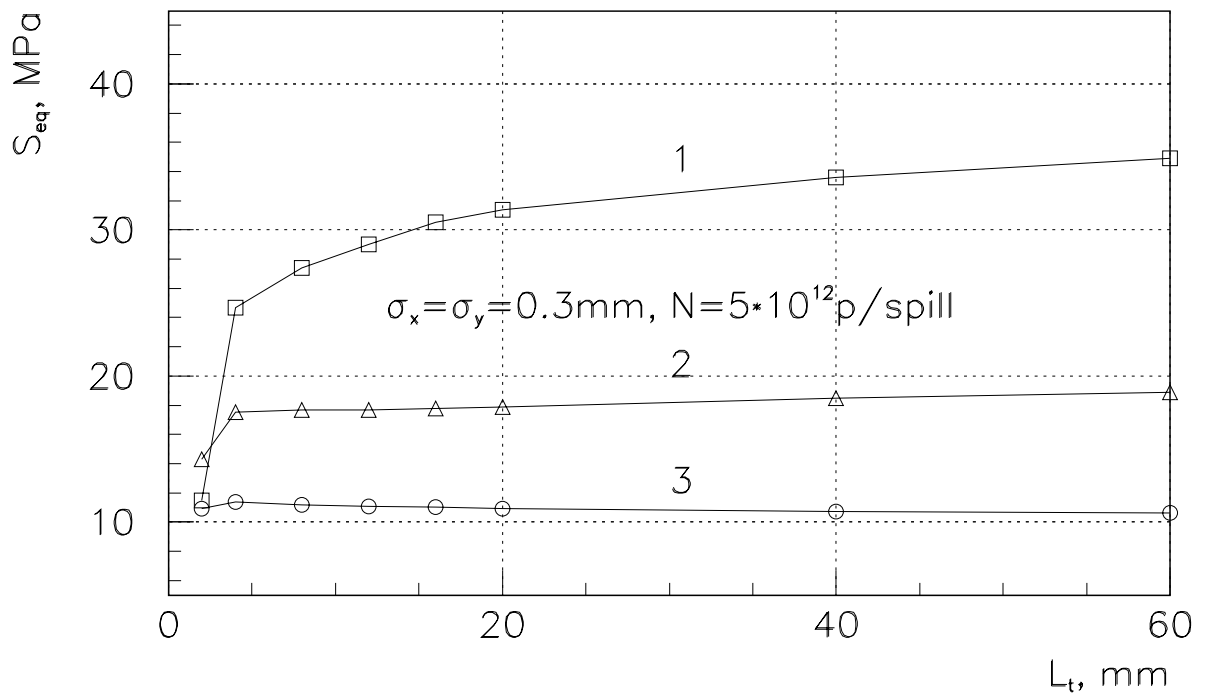


Figure 2.8: Equivalent stresses in different critical points of the target tooth in the graphite prototype as functions of the tooth length.

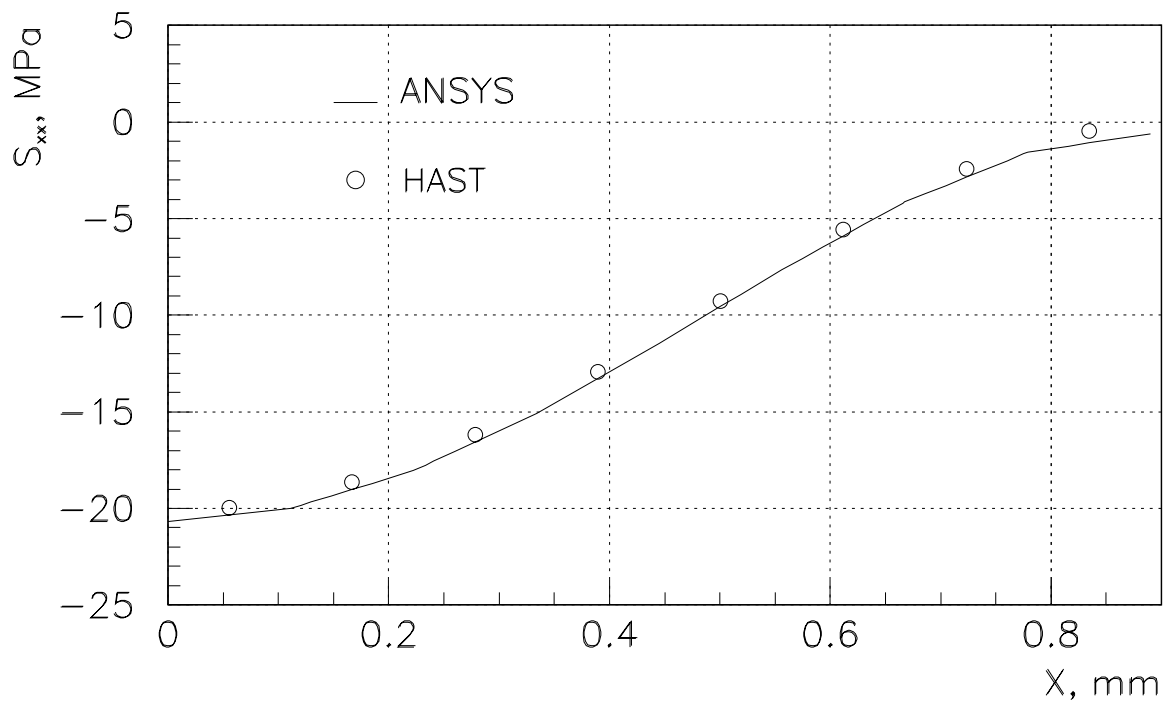
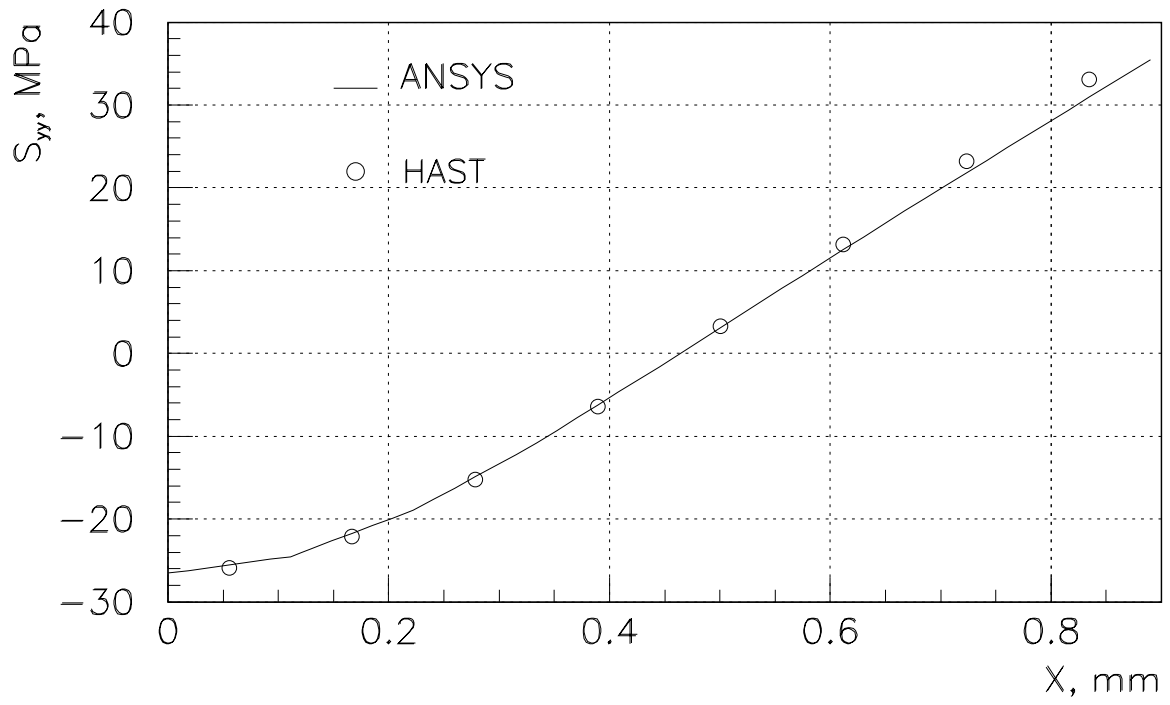


Figure 2.9: Stresses as function of X-coordinate at $y = z = 0$ computed by ANSYS and HAST.

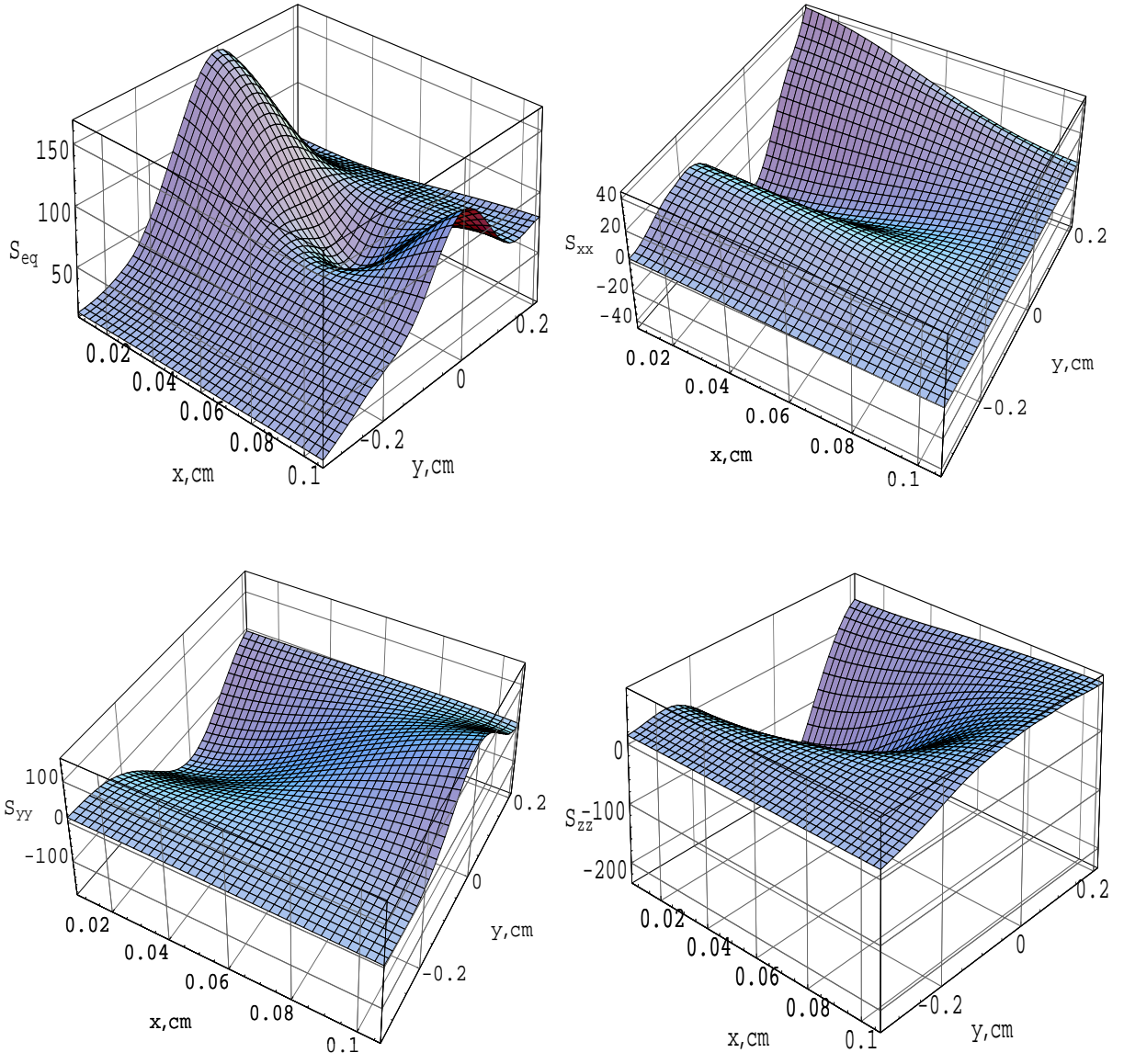


Figure 2.10: Stresses in the middle cross-section ($z = 0$) of the beryllium tooth ($1.0 \cdot 10^{13}$ p/spill).

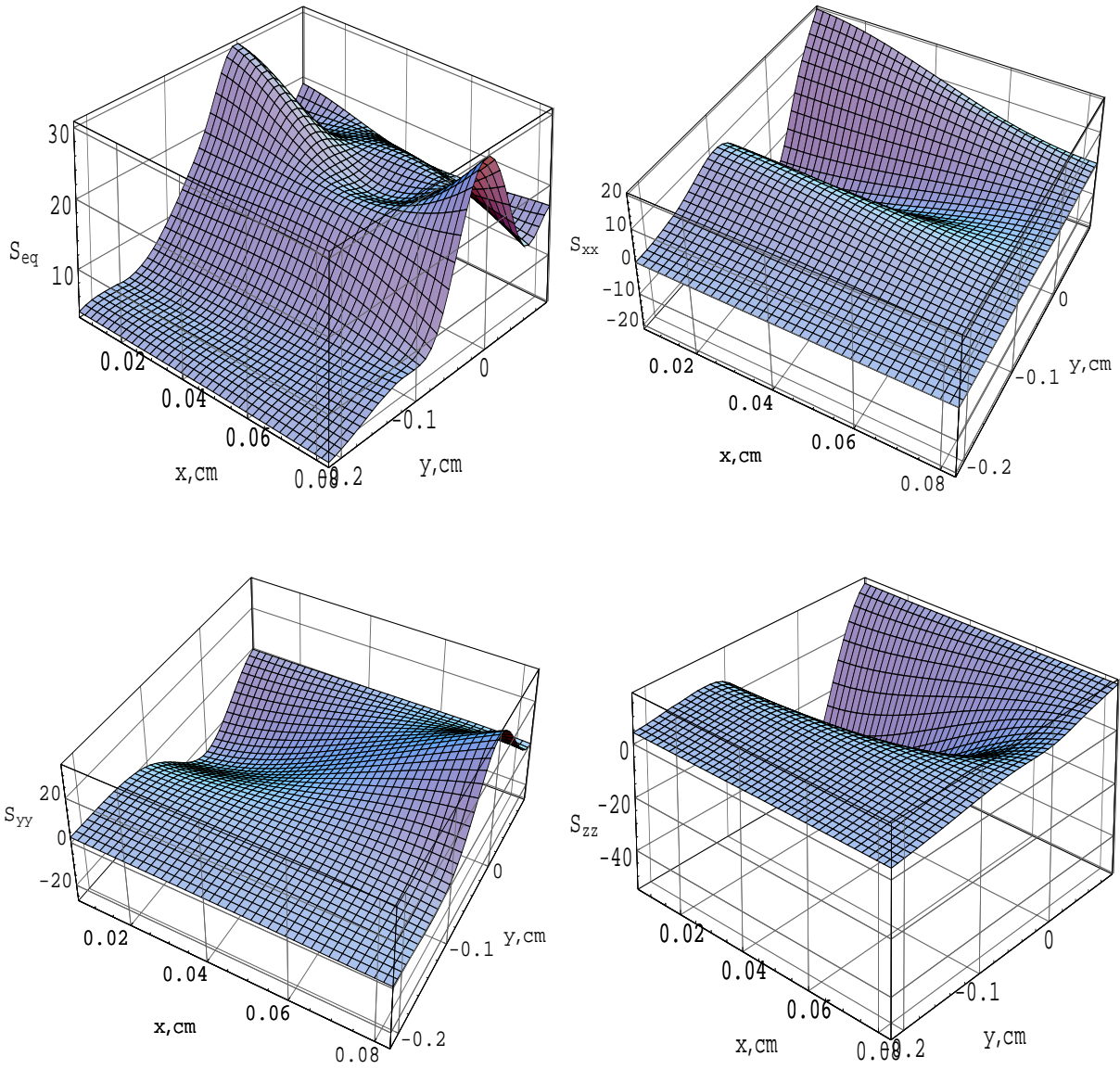


Figure 2.11: Stresses in the middle cross-section ($z = 0$) of the graphite tooth ($1.0 \cdot 10^{13}$ p/spill).

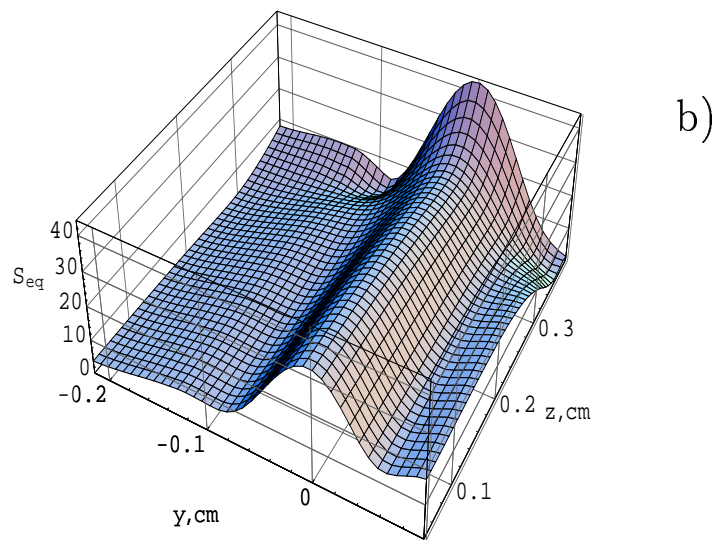
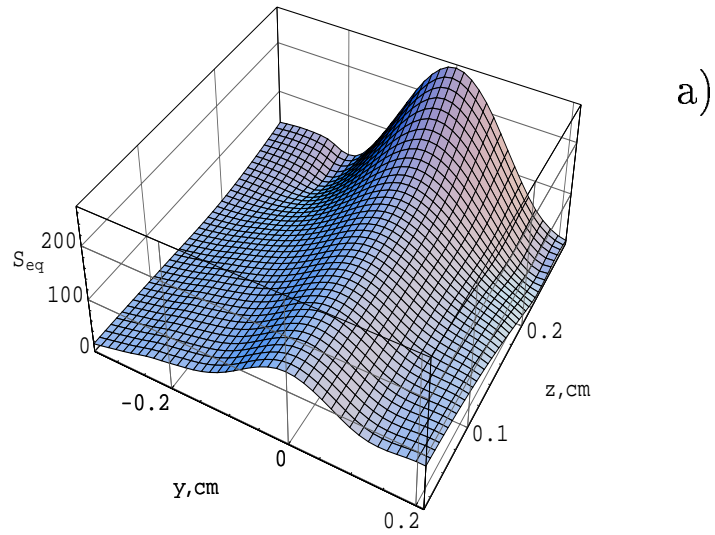


Figure 2.12: Distributions of equivalent stress in YZ-plane for $x = d/2$ ($1.0 \cdot 10^{13}$ p/spill): a) beryllium; b) graphite.

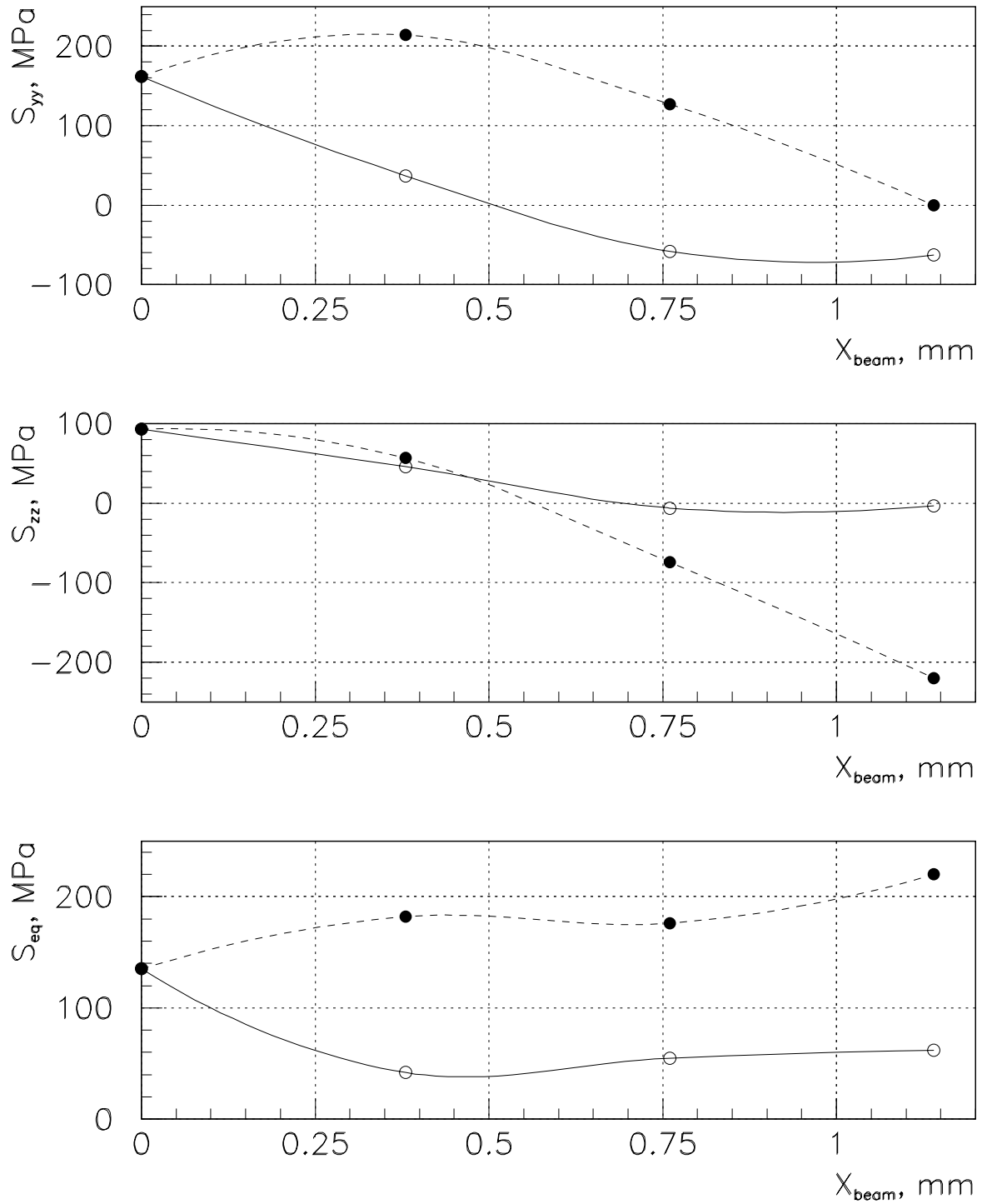


Figure 2.13: Stresses in the beryllium target tooth as function of the beam center location ($1.0 \cdot 10^{13}$ p/spill): solid lines correspond to the point $(-d/2; 0; 0)$, dashed lines correspond to the point $(d/2; 0; 0)$.

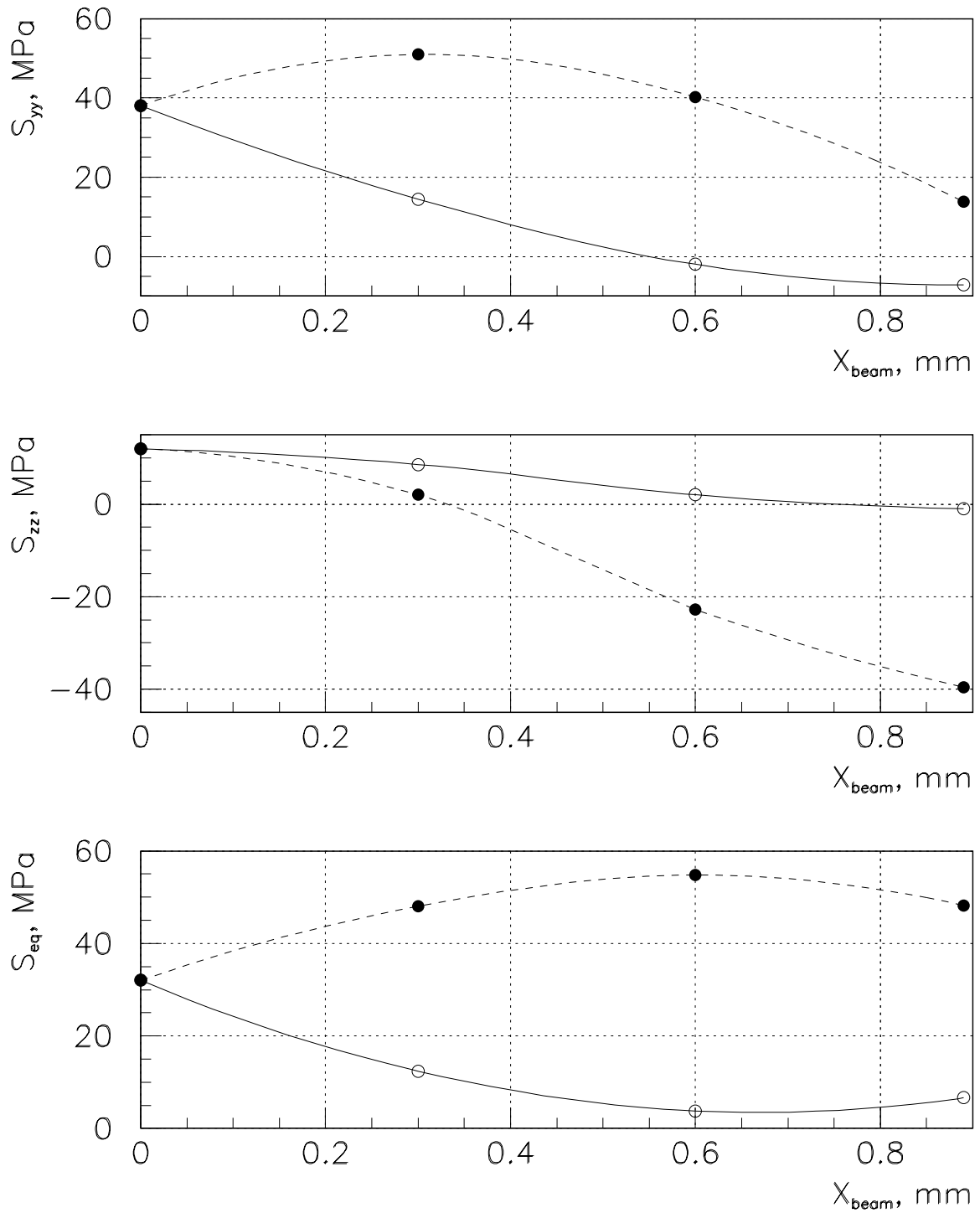


Figure 2.14: Stresses in the graphite target tooth as function of the beam center location ($1.0 \cdot 10^{13}$ p/spill): solid lines correspond to the point $(-d/2; 0; 0)$, dashed lines correspond to the point $(d/2; 0; 0)$.

3 Neutrino Beam Optics

3.1 Low Energy Wide Band Beam

The possibility of producing a WBB at the MINOS far detector in the neutrino energy range lower than that for the H6.6 three horns focusing system [11], optimized for the energy range of 8–24 GeV, has been considered in the IHEP Task B Report [18]. Two types of focusing systems, the first with two parabolic shaped horns (PH2) and the second with three conical shaped horns (CH3), were investigated for the energy range of $E_\nu < 12$ GeV. All horns in both focusing systems are powering in series with the current of 200 kA. One meter long and 4 mm in diameter graphite target was used for the pions production.

Both PH2 and CH3 focusing systems give a significant increase (factor 1.7–1.8) of the ν_μ event rate in the energy range of 3–9 GeV with respect to the H6.6 baseline design, although the total ν_μ event rates for both low energy designs are only 0.4–0.6 of that for the H6.6. Changing only the target and horn locations, the PH2 and CH3 focusing systems with the same horn currents may be also used for obtaining of neutrino beams in significantly higher energy range covered by the H6.6 design.

On the other hand, to improve the MINOS sensitivity to neutrino oscillations in the region of low Δm^2 (a few $\times 10^{-3}$ eV²), one should increase neutrino event rate in the energy range of a few GeV. This Section describes results of the beam optics study for the 1–5 GeV neutrino beam based on the parabolic shaped horns, optimized earlier for the PH2 focusing system.

Figure 3.1 shows the schematic of the PH2 optics design modified to obtain more low energy neutrino beam. This new focusing system labelled as PH2le is significantly shorter than original PH2 design: the distance between two horns is equal to 6 m instead of 18 m for the PH2. As for the previous considered PH2 focusing systems, the horn feeding current is equal here to 200 kA, which gives the possibility to have the same power supply system for all considered variations of the PH2 optics design.

Two interaction lengths beryllium target with the diameter of 6.4 mm is located entirely inside the first horn in order to accept the low momenta pions at large angles. The depth of the focus for the PH2le design is shown in Figure 3.2. It was obtained by the event rate calculation at the far detector for different locations of a point-like target along Z-axis. All

curves are normalized so that 1.0 is the highest point of the curve for the neutrino energy range of 4–5 GeV. As follows from these plots, even more short and more dense target will be better to produce neutrino beam in very low energy range. In any case, a final choice of the target parameters for such neutrino beam should be followed by designs of the target mechanical support and cooling systems.

The ν_μ charged current event rate at the far detector calculated using the Fermilab GNUMI beam simulation software for the PH2le focusing system and that for the original (medium energy) PH2 design are shown in Figure 3.3. Table 3.1 gives the total ν_μ charged current event rate for these focusing systems in different neutrino energy ranges. Despite a relatively smaller overall event rate, the PH2le focusing system produces twice as high neutrino events in neutrino energy range $E_\nu < 3$ GeV than the PH2. At the same time, the PH2le spectrum has only 45% of the neutrino events with the energy $E_\nu < 6$ GeV. The remaining events give the high energy tail, which form a background in such neutrino beam.

Focusing systems	Number of ν_μ events per kTon·Yr in the energy range of			
	$E_\nu < 3$ GeV	$E_\nu < 6$ GeV	$E_\nu > 6$ GeV	Total
PH2	48	460	1016	1476
PH2le	91	194	242	436
PH2le+plug	87	187	111	298

Table 3.1: The ν_μ charged current event rates at the far detector in different neutrino energy ranges.

In order to suppress this high energy tail, the beam plug should be located in the focusing system to absorb the high energy secondaries moving through the focusing system in the vicinity of the beam axis. Figure 3.4 and the last row of Table 3.1 illustrate the effect of the 1 m long and 15 mm radius beryllium plug located in the PH2le focusing system after the first horn. As it follows from these results, the beam plug effectively decreases the high energy part of neutrino spectrum (the number of neutrino events with the energy $E_\nu > 6$ GeV reduces from 242 to 111), while the low energy part of neutrino spectrum remains without visible changes.

In addition, the beam plug has a positive influence to the $\tilde{\nu}_\mu$ component of the background. Data from Table 3.2 indicate the significant increase of the $\tilde{\nu}_\mu$ background for the PH2le focusing system with respect to the medium energy PH2 design. The PH2le+plug focusing system half as much decrease the number of $\tilde{\nu}_\mu$ charged current events at the far detector, intercepting the flux of high energy negative secondaries passing to the decay region through field free holes in horn necks. The $(\nu_e + \tilde{\nu}_e)$ component of background arising from K^\pm and μ^\pm three-body decays remains for both modifications of low energy designs at the same level as for the PH2.

Contamination	PH2	PH2le	PH2le+plug
ν_μ	1476 (96.0%)	436 (87.2%)	298 (90.8%)
$\tilde{\nu}_\mu$	47.0 (3.06%)	58.7 (11.7%)	25.3 (7.71%)
ν_e	14.1 (0.92%)	4.53 (0.91%)	4.15 (1.26%)
$\tilde{\nu}_e$	0.91 (0.06%)	0.90 (0.18%)	0.67 (0.20%)

Table 3.2: Neutrino charged current event rates at the far detector.

3.2 Narrow Band Beam

As it follows from previous IHEP Reports, the WBB focusing system consisting of two sets of magnetic horns (with parabolic or conical shaped inner conductors) with addition of some dipoles, collimators and a primary proton beam dump may be also used to produce a NBB. Proposed beam optics design [19] allows to use an identical focusing devices (FD) and the same power supply system for both wide and narrow band beams and to have a rather simple change between two types of neutrino beams.

The horns with parabolic shaped inner conductors (parabolic lenses), which have been elaborated and produced at IHEP for the 70 GeV WBB, were considered for the first time as a possible variant of the FDs. The schematic of such beam optics is given in Figure 3.5; each focusing device here is the assembly of two bolted together parabolic lenses. The main geometrical dimensions of parabolic lenses which have been used for designing of the NBB focusing system and electrical parameters of both FD1 and FD2 are given in [19, 20].

Considered parabolic lens focusing system, labelled as 2LX/2B/2L3, provides the NBB with the parent particle momenta from 20 GeV/c up to

45 GeV/c. Tuning to different momenta was planned to be done here by changing the currents in parabolic lenses and dipoles, while the target and all equipment would stay at fixed positions. The currents I_1/I_2 are equal to 320/320 kA for 20 and 45 GeV/c tunes and 320/190 kA for 30 GeV/c tune. Due to relatively large depth of the focus, this optics allows to use a low density graphite or beryllium target.

The beam absorber is located in the NBB optics to absorb both non-interacted with the target primary protons and secondary particles which are out of the useful beam, and to transfer their energy to the water cooling loop. The total length of the absorber is equal to 4.4 m. Its first part (corebox) consists of eight 0.25 m long and 160 mm in diameter graphite cylinders, which are held in 3 m long water-cooled aluminum jacket. The second part of the beam absorber is 1.4 m long steel shielding, which was included in the design to absorb the energy flux emitted from the back end of the corebox and to reduce an irradiation of the B3 magnet coils. The conceptual design of the beam absorber is given in [18] and is taken into account in all subsequent considerations of the NBB optics designs.

Following to general idea of such beam optics design, the PH2 focusing system with two parabolic shaped horns may be also rearranged to produce a NBB. Below a preliminary results are given for the PH2he modification of the PH2. The location of the momentum selection section (B1 ÷ B3 and the beam absorber) with respect to the first horn for the PH2he/NBB design is the same as for the 2LX/2B/2L3 (see Figure 3.5). The second horn of the PH2he/NBB is located ~ 10 m downstream the FD2 of the 2LX/2B/2L3. There are two possible ways to tune such beam optics to various momenta:

- by changing the position of the target and scaling currents in dipoles, keeping currents in parabolic horns constant;
- by changing currents in parabolic horns and scaling currents in dipoles, keeping the target at fixed position.

In both cases the positions of parabolic horns and momentum selection section were retained unchanged. The first way gives the highest acceptance for all tunes, while the second one simplifies tuning to various momenta.

Figure 3.6 illustrates the possibility of producing the NBB with different parent particles momenta for the PH2he optics design in the case of a target position adjustment. These results were obtained using Monte Carlo

program HALO [21] modified for fast calculations of neutrino beam spectra at the far detector. The hadron production model based on the Malensek formula [22] is used in this program. The locations of the 0.5 m long graphite target with the radius of 2 mm, which was used in these beam simulations for different NBB tunes are given in Table 3.3, as well as the total ν_μ charged current event rate at the far detector.

PH2he/NBB tune, GeV/c	Target position, m	Total ν_μ event rate per kTon·Yr
10	-0.65	70
15	-1.40	172
20	-1.70	237
30	-2.40	352
45	-2.90	470

Table 3.3: Positions of the target center and the total ν_μ event rate for different NBB tunes ($z = 0$ is upstream end of Horn#1).

More detail study of the NBB performance of the PH2 optics design, including the minimizing of the low energy tail of neutrino energy spectrum, should be done using the GNUMI software taking into account the production of secondaries in the collimators, decay pipe and horn walls. Figure 3.7 shows the ν_μ charged current event rate at the far detector calculated using the GNUMI for the PH2he/NBB and 2LX/2B/2L3 focusing systems in the case of 45 GeV/c tune.

As it follows from these neutrino beam simulations, the PH2he/NBB focusing system in its preliminary approach gives more narrow neutrino energy spectrum and $\sim 20\%$ smaller total ν_μ charged current event rate with respect to the 2LX/2B/2L3 design. The number of neutrino events with $E_\nu < 10$ GeV is equal to 3.6 for both focusing systems, which gives 0.56% and 0.46% of the low energy tails for the PH2he/NBB and 2LX/2B/2L3 designs respectively.

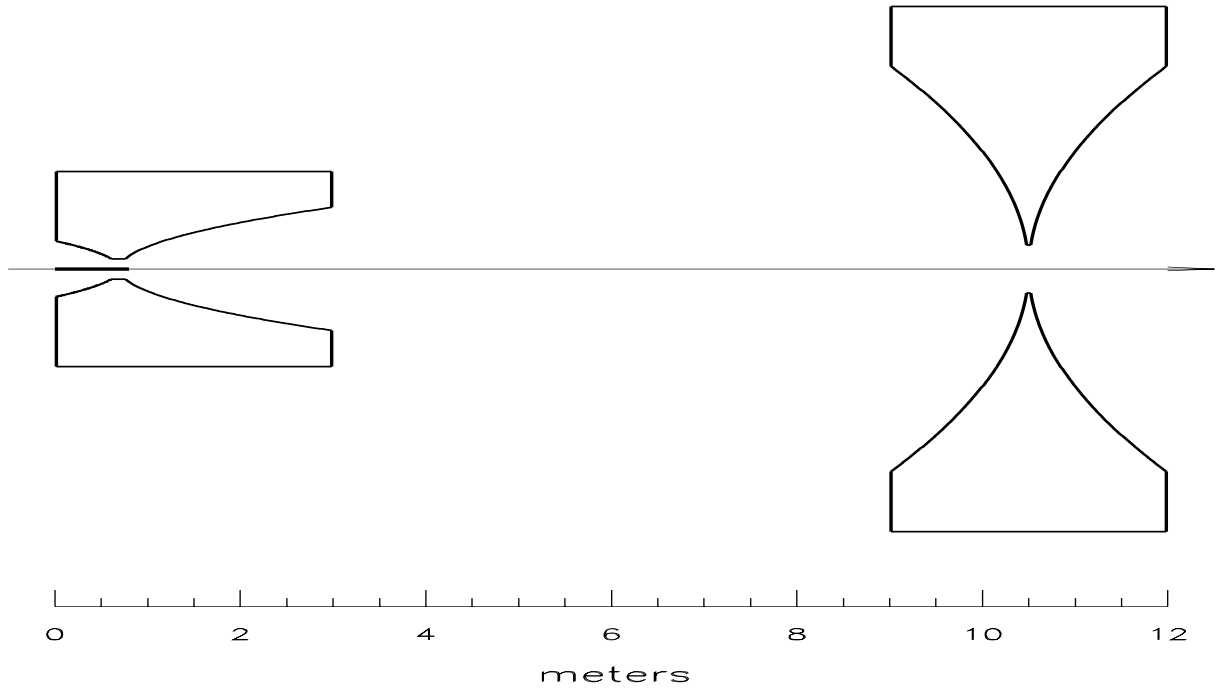


Figure 3.1: Schematic of the PH2le optics design.

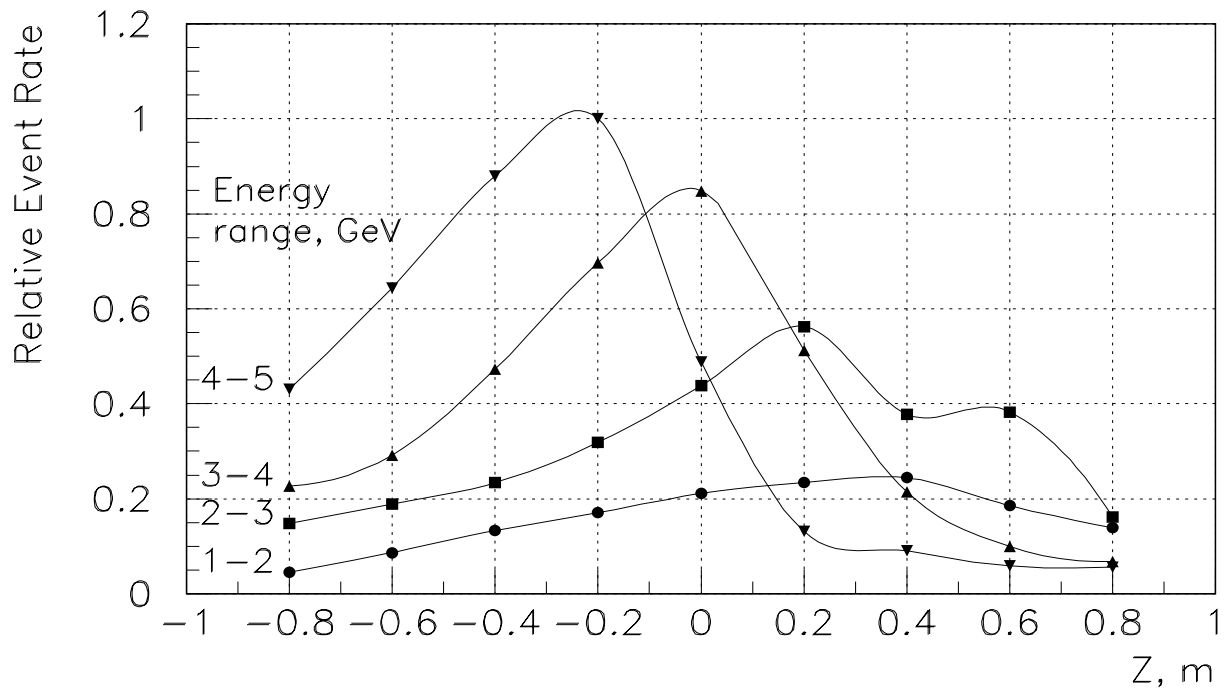


Figure 3.2: Depth of a focus in different neutrino energy ranges for the PH2le design ($z = 0$ is upstream end of Horn#1).

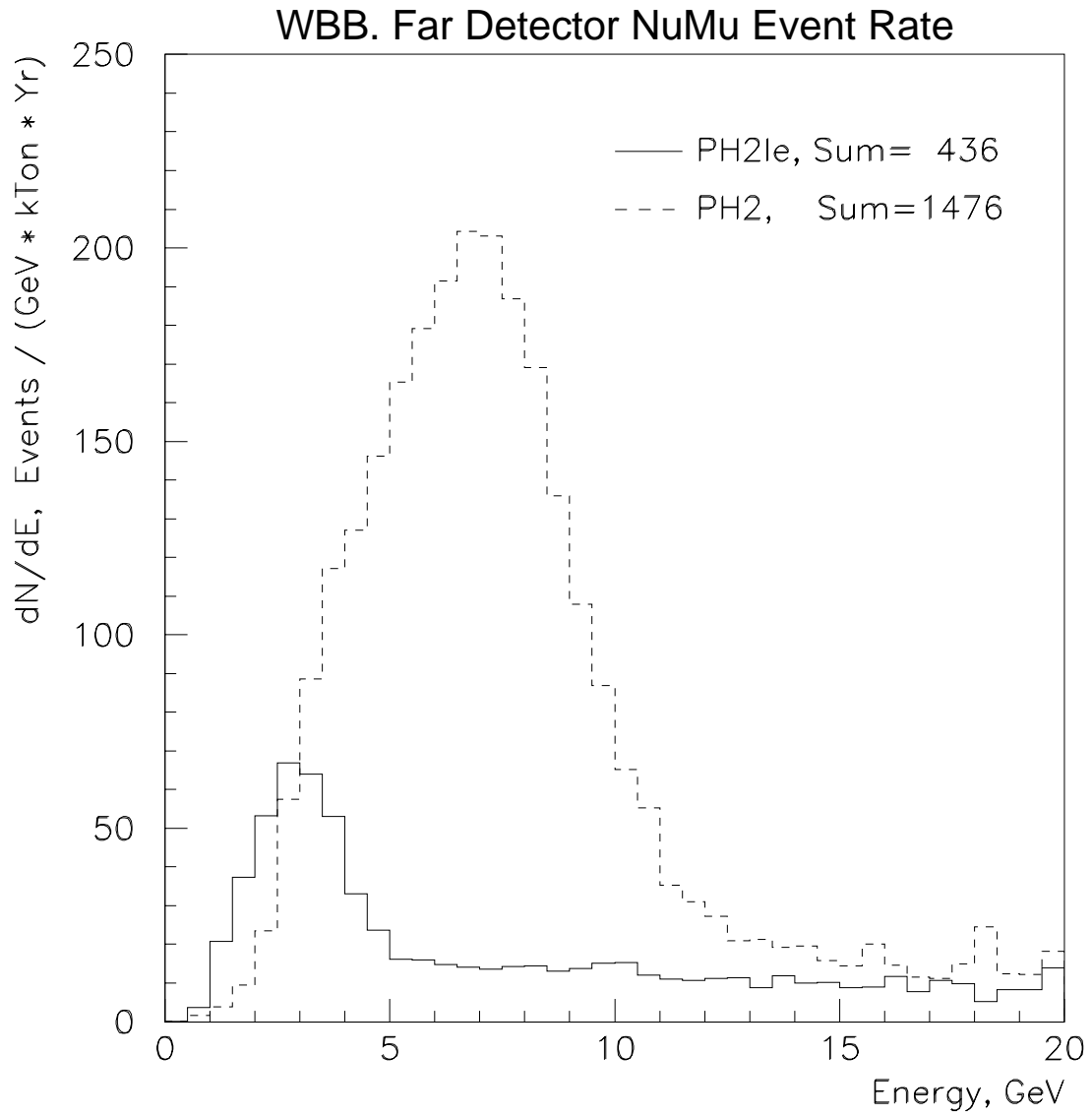


Figure 3.3: The ν_μ charged current event rates for the PH2le and PH2 optics designs.

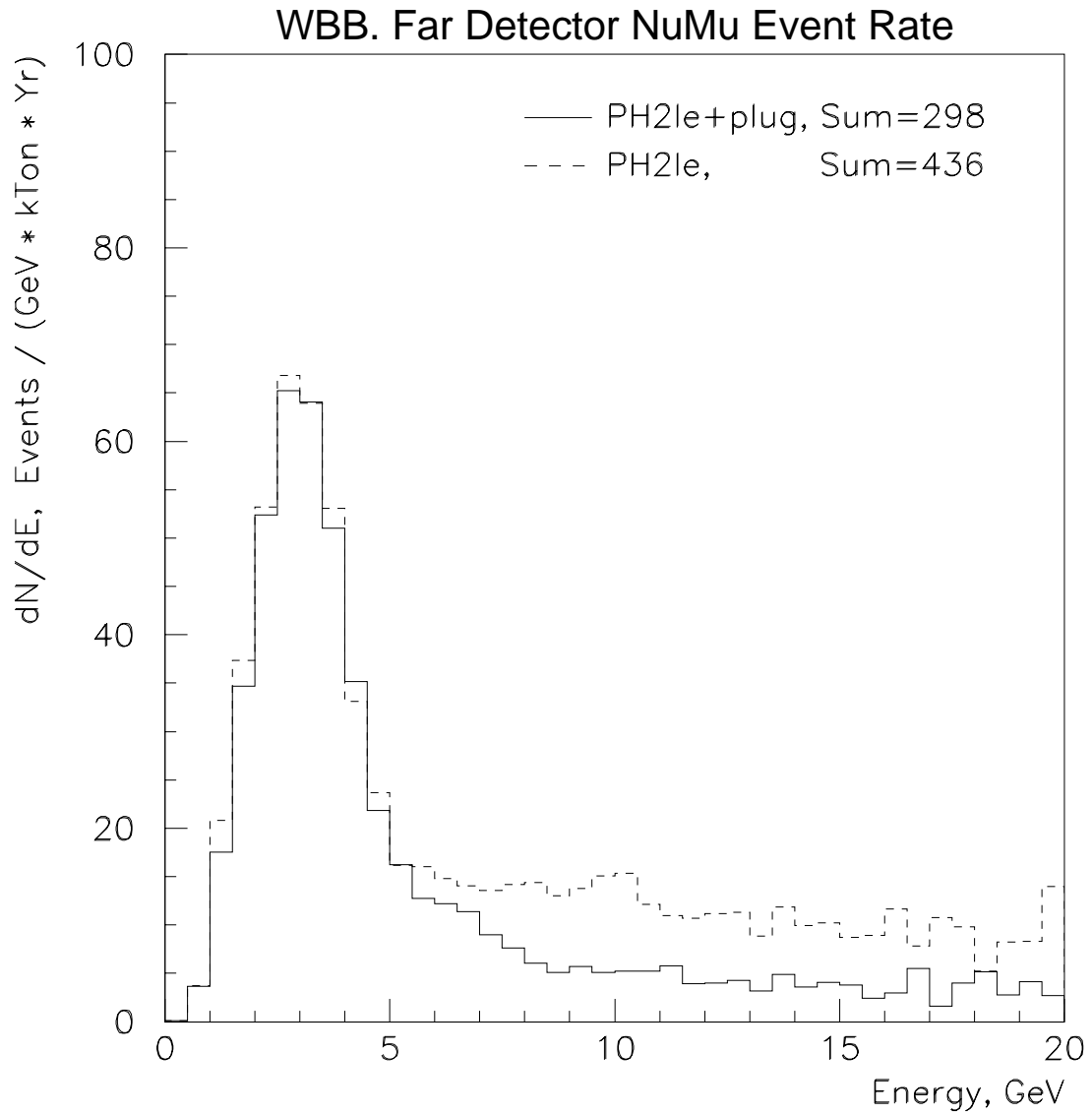
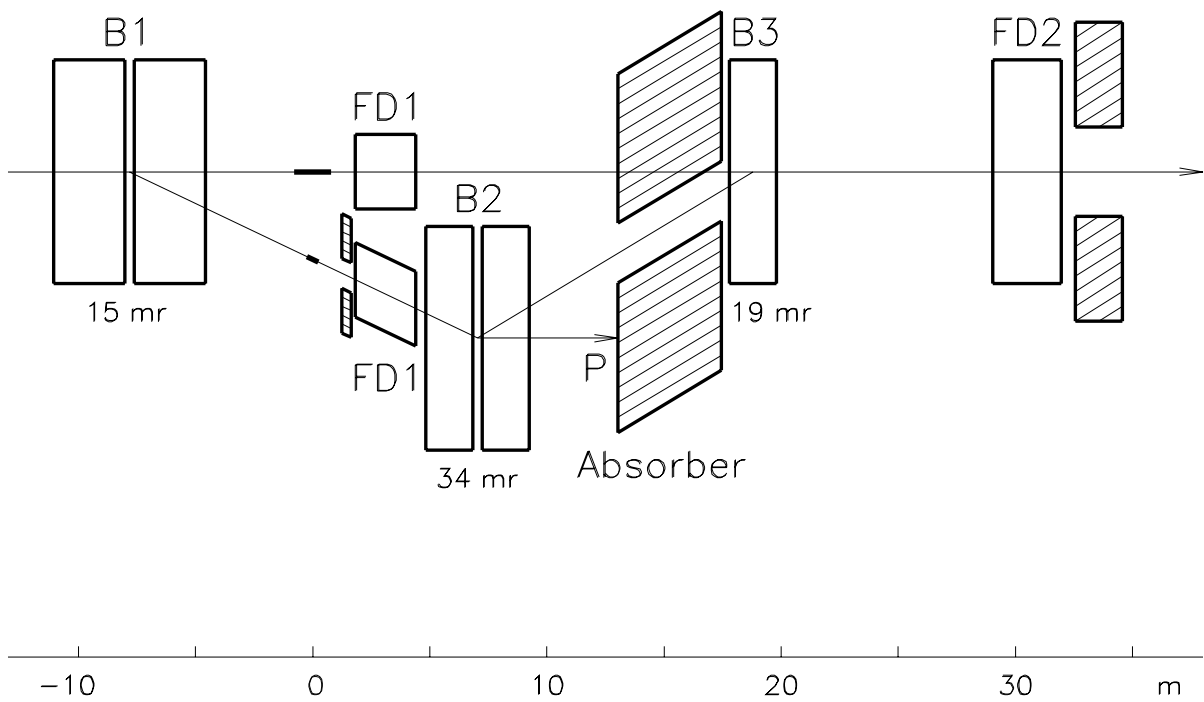


Figure 3.4: The ν_μ charged current event rates for two modifications of the PH2le optics design.

WBB and NBB Layout

(Not to Vertical Scale)



Dipole Aperture (W x G): B2 – 12cm x 10cm
B3 – 17cm x 13cm

Figure 3.5: Schematic of the WBB/NBB optics designs.

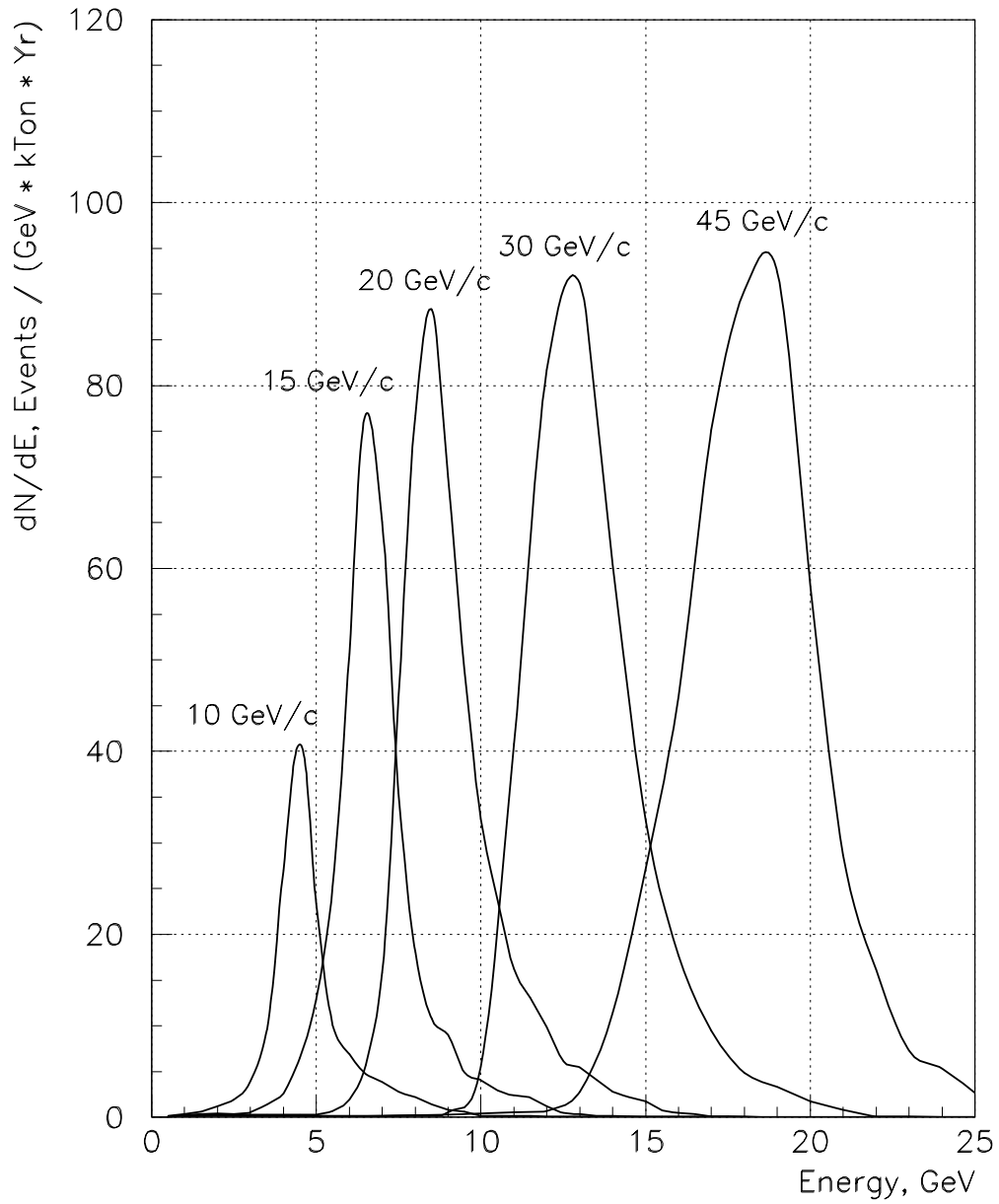


Figure 3.6: The ν_μ charged current event rate at the far detector for the PH2he/NBB optics design calculated using HALO.

NBB. Far Detector NuMu Event Rate.

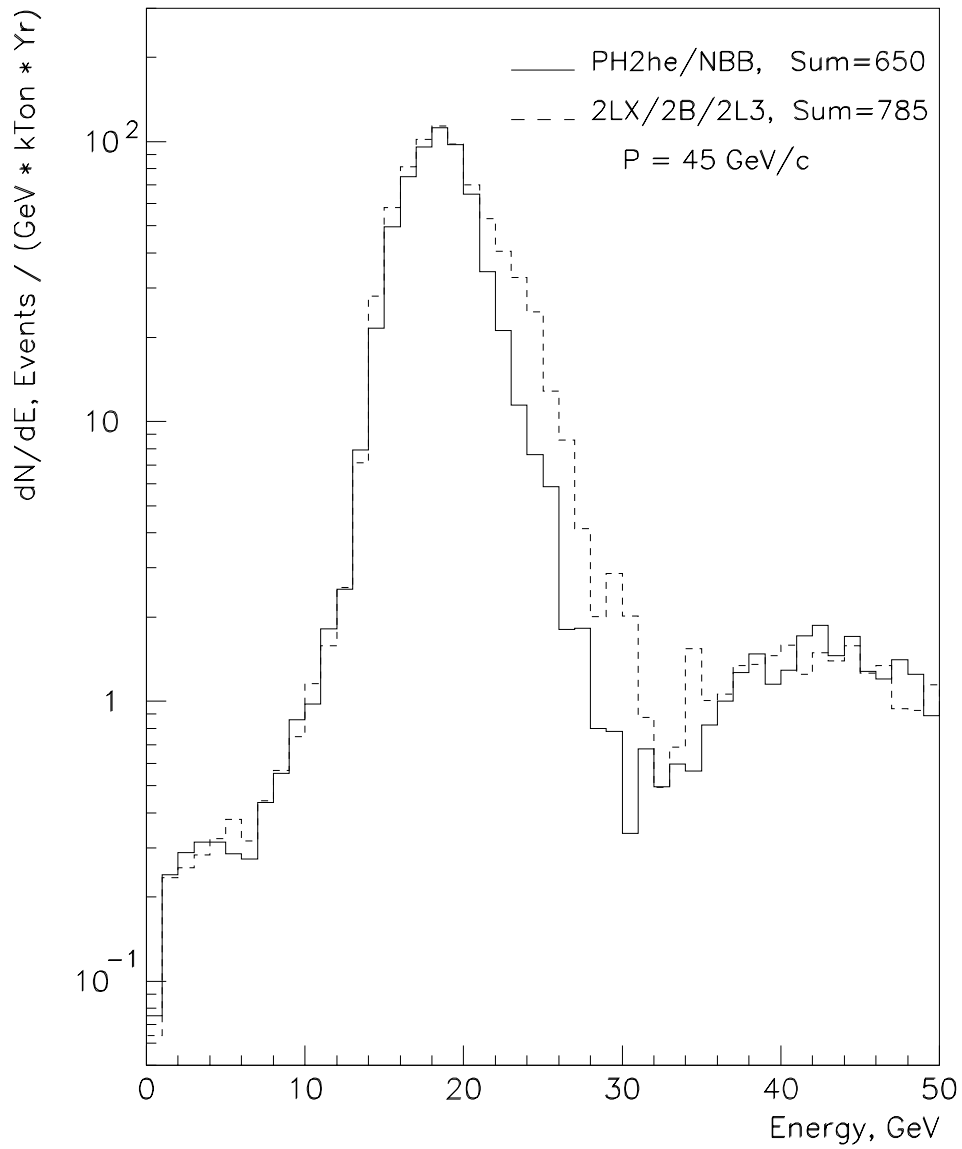


Figure 3.7: The ν_μ charged current event rate at the far detector for the PH2he/NBB and 2LX/2B/2L3 optics designs in the case of 45 GeV/c tune calculated using GNUMI.

References

- [1] Graphite Materials for Industrial Applications, Poco Graphite, Inc., A Unocal Company, 1601 South State Street, Decatur, Texas 76234.
- [2] Properties and Characteristics of Graphite, Edited by W.H.Brixius, March 1994, Poco Graphite, Inc., A Unocal Company, 1601 South State Street, Decatur, Texas 76234.
- [3] Pre-engineering Design of the Technical Components, Task D IHEP Report, Protvino, 1997.
- [4] Brush Wellman Inc., Engineered Materials. 17876 St. Claire Avenue, Cleveland Ohio 44110.
- [5] D.E.Dombrowski, E.Deksnis, M.A.Pick "Thermomechanical properties of Beryllium", TR-1182, v.5 of the Series "Atomic and Plasma - Material Interaction Data for Fusion", February 20, 1995, Int.At.En.Agency, Vienna, Austria.
- [6] R.D.Watson, D.L.Youchison, D.E.Dombrowski, R.E.Guiniatouline, I.B.Kupriynov "Low Cycle Thermal Fatigue Testing of Beryllium Grades for ITER Plasma Facing Components", 2-nd IEA Int'l Workshop on Be Technology for Fusion, September 6-8, 1995, Jackson Lodex, Wyoming.
- [7] "The fabrication of beryllium, Vol.1: A Survey of Current Technology", NASA, MSCF, Huntsville, Alabama, NASA-TMX-53453, July 1966.
- [8] J.Hylen, Private communication.
- [9] Degtyarev I.I. et al., IHEP Preprint 94-119, Protvino, 1994.
- [10] A.Abramov et al., IHEP Preprint 84-64, Serpukhov, 1984.
- [11] A.J.Malensek, Neutrino Beams Using the Main Injector, FNAL-TM-1951, Batavia, 1995.
- [12] Standard of Russian Federation Department of Atomic Energy, N95503, Moscow, 1984.
- [13] I.Azhgirey et al., Proc. XV Conference on Charged Particles Accelerators, p.74, Protvino, 1996.

- [14] V.A.Grigoriev, V.M.Zorin, "Heatenergetic and Heattechnique", v.2, (Russian edition), Moscow, 1988.
- [15] Status Report: Technical Design of Neutrino Beams for the Main Injector (NuMI), FNAL-TM-1946, NuMI-B-92, Batavia, 1995.
- [16] K.Anderson, Private communication.
- [17] Preliminary Design Work on NBB Absorber and Target Prototype, Task A IHEP Report, Protvino, 1998.
- [18] Conceptual Design of NBB Absorber and Low Energy WBB Calculations, Task B IHEP Report, Protvino, 1998.
- [19] Conceptual Design Work and Neutrino Beam Calculations, Task C IHEP Report, Protvino, 1997.
- [20] Preliminary Design Work and Neutrino Beam Calculations, Tasks A and B IHEP Report, Protvino, 1997.
- [21] Ch.Iselin, Preprint CERN 74-17, Geneva, 1974.
- [22] A.J.Malensek, FN-341, Batavia, 1981.